Aerospace Science and Technology 178 (2026) 113063

Contents lists available at ScienceDirect

Aerospace Science and Technology

journal homepage: www.elsevier.com/locate/aescte

Original article

# Reliable buckling load prediction for Ariane 6 test article: Experimental validation of the vibration correlation technique

Felipe Franzoni [a,*], Theodor Dan Baciu [a,b,c], Richard Degenhardt [a,b,c], Adrian Gliszczyński [b,d], Klaus Stromer [e], Jens Hornschuh [f], Kaspars Kalnins [g], Eduards Skukis [h], Jochen Albus [i]

[a] DLR, Institute of Lightweight Systems, Braunschweig, Germany
[b] PFH, Composite Engineering, Campus Stade, Stade, Germany
[c] University of Bremen, Faserinstitut Bremen e.V., Bremen, Germany
[d] Lodz University of Technology, Faculty of Mechanical Engineering, Department of Strength of Materials, Lodz, Poland
[e] MT Aerospace AG, Augsburg, Germany
[f] IMA Materialforschung und Anwendungstechnik GmbH, Dresden, Germany
[g] IC3 Ltd, Ogre District, Latvia
[h] RTU, Riga Technical University, Institute of Chemistry and Chemical Technology, Riga, Latvia
[i] ArianeGroup GmbH, Bremen, Germany

A R T I C L E I N F O

Communicated by Namilae Sirish

*Keywords:*
Buckling
Vibration correlation technique(VCT)
Imperfection-sensitive structures
Cylindrical shells
Launch vehicle structures
Full-scale qualification test
Non-destructive evaluation

A B S T R A C T

The recent progress of the vibration correlation technique (VCT) has consolidated its viability as a non-destructive experimental procedure for determining the in situ buckling load of unstiffened and skin-dominated stiffened downscaled cylindrical shells. Building on this foundation, the present paper aims to further validate the technique for full-scale, qualification-relevant applications, assessing its robustness in the context of design-proof testing of launcher structures. The specimen investigated is a full-scale launcher tank barrel, representative of the lower section of the hydrogen tank of Ariane 6 first stage. The barrel, composed of four aluminum panels welded together, was tested for buckling at IMA Dresden under the coordination of MT Aerospace AG (MTA) as part of Ariane 6 structural qualification campaign. The experimental campaign involved the first application of the VCT to full-scale buckling tests with combined axial–bending loads, carried out in two configurations: (1) using three out of four actuators evenly spaced around the circumference, and (2) using two actuators from the same setup. For each configuration, non-contact vibration measurements were taken at various load levels. These measured natural frequency variations, along with linear buckling loads obtained from finite element (FE) models, were used to evaluate the robustness and practical applicability of the VCT. The experimental results confirm VCT as a reliable non-destructive technique for estimating the buckling load of imperfection-sensitive, full-scale cylindrical shells. To complement the experimental investigations, a numerical framework is proposed, employing high-fidelity FE models with stochastic, Fourier-based imperfections and realistic loading via a UAMP subroutine in Abaqus, enabling reliable buckling predictions even in the absence of measured imperfection data.

## 1. Introduction

Qualification tests of full-scale shell structures are an essential part of the design of launch vehicles. This is true, especially for buckling-critical barrel structures, where the final design, including complicated stiffening and load diffusion elements, is verified through a buckling test, providing a better understanding of the buckling behavior and the primary factors affecting it [1]. In view of the destructive or terminal nature of the buckling experiments [2], including also the long production and test preparation cycles of barrel components, a specimen exclusively allocated to the static qualification test is required. From this perspective, there are inherent financial and time-consuming interests in the development and validation of nondestructive methods to obtain the in situ buckling load from the pre-buckling stage, like the vibration correlation technique (VCT) [3].

The VCT uses an initial model and measured data prior to buckling for estimating the buckling load of the structure, assuring a truly nondestructive experimental procedure. Typically, analytical or finite element

* Corresponding author.
*E-mail address:* Felipe.Franzoni@dlr.de (F. Franzoni).

https://doi.org/10.1016/j.ast.2026.113063
Received 12 January 2026; Received in revised form 5 May 2026; Accepted 25 June 2026
Available online 27 June 2026
1270-9638/

(FE) models of the nominal structure are considered as an initial model and the measured data consists of the natural frequency magnitudes associated with vibration tests performed at different axial compression load levels. Two classes of VCTs were established over the years: indirect and direct methods [2]. Indirect methods assess the actual boundary conditions for updating the initial model, improving the numerical estimation of the buckling load [4]. In contrast, direct methods fit a functional relationship—such as linear or quadratic—between the applied load and the loaded natural frequency, and then extrapolate this relationship to estimate the buckling load; see [5–7], among others.

The equivalence between the buckling load of a given structure and the load level in which the fundamental natural frequency is zero has been known for more than a century and it is accredited to Sommerfeld [8]. Yet, only in the 1950s, researchers explored this relationship for estimating the buckling load through a nondestructive experimental procedure [9,10]. The first VCT studies are based on the linear relationship between the axial load level and the square of the loaded natural frequency, analytically formulated for fully simply supported columns, plates [9], and cylindrical shells [11,12]:

$$f^2 + p = 1 \tag{1}$$

where $f$ is the ratio between the loaded natural frequency $\bar{\omega}_{mn}$ and the unloaded natural frequency $\omega_{mn}$, both associated with the same vibration mode defined by $m$ axial half-waves and $n$ circumferential waves (for cylindrical shells), and $p$ is the ratio between the applied load $P$ and the critical buckling load $P_{\mathrm{CR}}$ (from an eigenvalue buckling analysis or theoretical buckling equations). From Eq. (1), direct and indirect VCT approaches were established in the subsequent five decades [2]; a complete review of this research effort is available in the quoted book. For more recent developments, see chapter 2 of [3] and [13].

The classic direct VCT consists of plotting the characteristic chart $f^2$ versus $p$ and calculating a best-fit linear relationship between the experimental data. In this method, the buckling load is extrapolated as the load level associated with zero magnitude of the loaded natural frequency [2,9,10]. Even considering that the linear relationship does not hold in the presence of other than fully simply supported boundary conditions, the method delivers proper estimations for columns with different boundary conditions, where deviations from linearity between $f^2$ and $p$ are negligible, as demonstrated in the experimental campaigns [9,14,15].

From the bibliographic review [2], the classic VCT approach is shown to be straightforward for imperfection-insensitive structures. For example, Chailleux et al. [15] successfully estimated the buckling load of simply supported flat plate specimens with small imperfections in the 1970s. More recently, Chaves-Vargas et al. [16] applied the linear approach to flat carbon fiber-reinforced polymer stiffened plates. However, earlier studies by Lurie [9] did not validate the approach for simply supported flat plates, likely due to significant deviations from flatness in the specimens.

A multitude of modified VCTs addressing imperfection-sensitive structures like curved panels and cylindrical shells were devised by different authors [2]. In the 1970s, Radhakrishnan [5] extrapolated the final linear path of the classic characteristic chart to the applied load axis, obtaining exact results when using the last two measured points. Segal [17] investigated 35 existing VCT experiments of stiffened cylindrical shells. The author adjusted an optimal parameter to raise the natural frequency, for which a functional relationship to the main geometric characteristics of stiffened cylindrical shells was proposed. This study achieved a substantial reduction in the scatter of the VCT estimated knock-down factors (KDF) when compared to the indirect VCT method based on Eq. (1). This idea was further explored in [18], where the authors determined upper and lower bounds of the optimal parameter and, hence, of the estimated buckling load.

Preceding the methodology herein employed, Souza et al. [6] devised a VCT addressing imperfec-tion-sensitive stiffened cylindrical shells. In this method, a linear relationship must be adjusted in a modified characteristic chart based on the parametric forms $(1-p)^2$ and $1-f^4$, as presented in Fig. 1, which reproduces the results from [6].

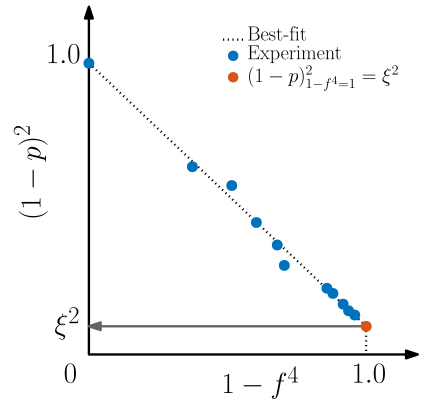


**Fig. 1.** Schematic representation of the VCT established in [6].

The buckling load is estimated by evaluating the parametric form $(1-p)^2$ when the loaded natural frequency is zero (i.e., $1-f^4=1$ in the frequency parametric form), which in turn, is expressed mathematically as:

$$(1-p)^2 + (1-\xi^2)(1-f^4) = 1 \tag{2}$$

where $\xi^2$ is the magnitude of $(1-p)^2$ when $1-f^4$ is equal to one, representing the square of the drop of the load-carrying capacity due to initial imperfections. From the estimated $\xi^2$, the VCT estimation of the buckling load $P_{\mathrm{VCT}}$ is:

$$P_{\mathrm{VCT}} = P_{\mathrm{CR}}(1-\sqrt{\xi^2}) \tag{3}$$

The term $1-\sqrt{\xi^2}$ in Eq. (3) is interpreted as an experimental estimation of the KDF $\gamma$ of conventional sizing approaches [19]. Alternatively, the authors proposed another method for stiffened cylindrical shells in [20], where the classic characteristic chart is approximated as a cubic parametric curve. Both methods [6,20] were validated considering experimental results of stiffened cylindrical shells tested at Technion [21]. Similarly, the classic characteristic chart was represented by a second-order equation in [22]. The authors adjusted the second-order best-fit relationship applied to curved stiffened panels. An assessment of the estimated buckling load accounting for load levels up to 50% of the linear buckling load showed reasonable results. Nevertheless, for improving the estimations, the authors suggested load levels near the typical sharp bend of the classic characteristic chart.

Following the methodology depicted in Fig. 1, Arbelo et al. [7] introduced a significant modification in 2014. The authors proposed a novel VCT approach based on evaluating a second-order relationship between the parametric forms $(1-p)^2$ and $1-f^2$, which has been empirically verified. Fig. 2 reproduces the results from [7] and provides a schematic illustration of this methodology.

The second-order equation is fitted from the experimental data and it is considered to evaluate $\xi^2$ as the minimum value of the $(1-p)^2$ axis. Mathematically, the method is formulated as:

$$(1-p)^2 = A(1-f^2)^2 + B(1-f^2) + C \tag{4}$$

where $A$, $B$ and $C$ are the fitting coefficients and, the $\xi^2$ is calculated as:

$$\begin{aligned} \min(1-p)^2 &= \xi^2 \\ &= -B^2/4A + C \end{aligned} \tag{5}$$

Equally to [6], $\xi^2$ from Eq. (5) is used for the buckling load estimation in Eq. (3). The applicability of this methodology depends not on the similarity between the buckling and vibration modes, but rather on the influence of initial imperfections on the loaded frequency magnitude.

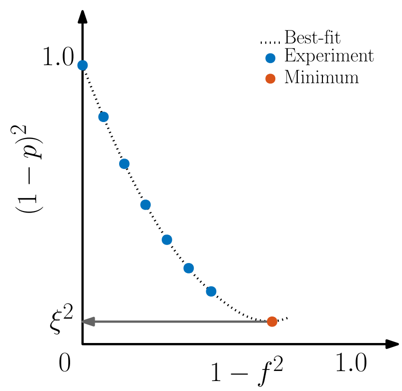


**Fig. 2.** Schematic representation of the VCT established in [7].

There are 8 experimental campaigns [23–30] that corroborate the applicability of this methodology for downscaled metallic and composite cylindrical shells with different design details: unstiffened [23–26], with and without cutouts [27], grid-stiffened [28], with closely-spaced stringers and internal pressure [29], and manufactured considering variable angle tow [30]. While the method was initially empirical, Franzoni et al. [31,32] subsequently provided analytical justification for the second-order relationship between $(1-p)^2$ and $1-f^2$, and proposed an interpretation for the definition of VCT using the minimum value of $(1-p)^2$. Following this development, several authors have extended this analytical verification to other structures, such as conical shells [33], combined load scenarios [34], and composite lattice sandwich cylinders [35].

More recently, Skukis et al. [36] conducted a detailed study that assessed the robustness of empirical methodologies by analyzing numerous experimental results for cylindrical shells. Moreover, Gliszczynski et al. [37] performed an extensive parametric study to evaluate the predictive capabilities of the VCT [7] when applied to axially compressed CFRP truncated cones. Concurrently, Zarei et al. [38] experimentally validated the applicability of the VCT for conical shells. Furthermore, an extension was proposed in [39] where the authors combined the numerical VCT with the combined approximation, demonstrating its effectiveness in three distinct analyses. In their recent work, Baciu et al. [40] presented a sensitivity analysis regarding the number of load steps and the maximum axial load level used in VCT predictions, while also quantifying the uncertainty associated with the measured natural frequency. Continuing this line of research, Baciu et al. [41] further explored VCT reliability in the presence of geometric and loading imperfections, whereas Baciu et al. [42] investigated the influence of combined loading.

Additionally, Franzoni et al. [43] introduced an enhanced VCT for unstiffened composite cylindrical shells, and da Silva et al. [44] demonstrated the effectiveness of VCT in the numerical investigation of a large-scale sandwich structure, paving the way for full-scale applications. More recently, Gliszczynski et al. [45] extended the methodology to double-curved shells, showing through a comprehensive numerical study that VCT-based predictions remained consistently conservative across the investigated imperfection scenarios for such structures. In a subsequent contribution, Gliszczynski et al. [46] evaluated the robustness of VCT predictions for unstiffened CFRP cylinders under varied imperfection scenarios, confirming stable and reliable behavior. Moreover, Gliszczynski [47] further investigated the influence of boundary condition modeling and the choice of reference bifurcation load on VCT-based buckling predictions, demonstrating that analytically derived bifurcation loads slightly enhance the robustness and consistency of the method, yielding results comparable to those reported by Franzoni et al. [43].

Building on the recent developments of the VCT applied to downscaled cylindrical shells and the numerical investigations on a large-scale sandwich structure by da Silva et al. [44], this article further expands the applicability of the methodology [7] to a full-scale, flight-representative launcher barrel. The experiment, a buckling qualification test of a metallic structure representative of the Ariane 6 lower-stage hydrogen tank, was performed at IMA Dresden under the coordination of MTA. In addition to the required qualification test program, an exploratory VCT campaign was carried out, marking the first implementation of VCT within a launcher qualification test. The experimental results are employed to verify the VCT as a reliable and qualification-relevant non-destructive procedure for estimating the buckling load of imperfection-sensitive, full-scale cylindrical shells. Concurrently, the article presents a complementary numerical framework designed to replicate the qualification test conditions, using high-fidelity FE models with stochastic, Fourier-based imperfections and realistic loading via a UAMP subroutine in Abaqus. This approach enables reliable buckling predictions even in the absence of measured imperfection data, thereby broadening the practical applicability of numerical assessment.

## 2. Test article and load cases

This section provides an overview of the test article and the load cases. Firstly, it provides a full description of the specimen, including manufacturing and design details, followed by a definition of the load cases and their respective loading schemes.

### 2.1. Test article

The lower liquid propulsion module (LLPM) LH2 tank houses the cryogenic liquid hydrogen propellant for the lower module of the Ariane 6. The tank comprises four circumferentially friction stir-welded cylindrical barrels (numbered 1 to 4 from bottom to top), each consisting of four longitudinally friction stir-welded panels made from AA2219-T87 aluminum alloy. The test structure consists of a customized hybrid cylindrical shell composed of:

- Basis panel: a smooth panel without local reinforcements, corresponding to two panels from barrels 1, 2, and 3;
- Panel A: panel from barrel 2 including two local reinforcements (pad-ups);
- Panel B: panel from barrel 3 including three local reinforcements (pad-ups); and
- Panel C: panel from barrel 1 including three local reinforcements (pad-ups).

These local reinforcements (pad-ups) correspond to regions of increased thickness introduced for structural and functional purposes (e.g., load introduction, attachments, or interfaces), and result in localized stiffness variations that influence the structural response. The four curved panels were also manufactured from AA2219-T87 aluminum alloy and, unlike the original structure, were welded together using the TIG process. This deviation from the flight-representative configuration was dictated by manufacturing constraints of the test article. Compared to friction stir welding (FSW), TIG welding produces larger heat-affected zones (HAZ), which can induce higher residual stresses, greater geometric distortions, and more pronounced local degradation of mechanical properties. As a result, the TIG-welded joints may exhibit reduced local stiffness and strength, as well as increased imperfection amplitudes in the weld vicinity. These features are known to affect the buckling behavior of thin-walled shells, primarily through increased imperfection sensitivity. Within the scope of this study, the test article is therefore considered representative of a realistic as-built configuration, and the measured structural response inherently incorporates these manufacturing-induced effects.

The nominal thickness $t$ of the panels is 2.55 mm, the axial length of the barrel is 3110 mm, and its nominal inner diameter is 5400 mm. Fig. 3

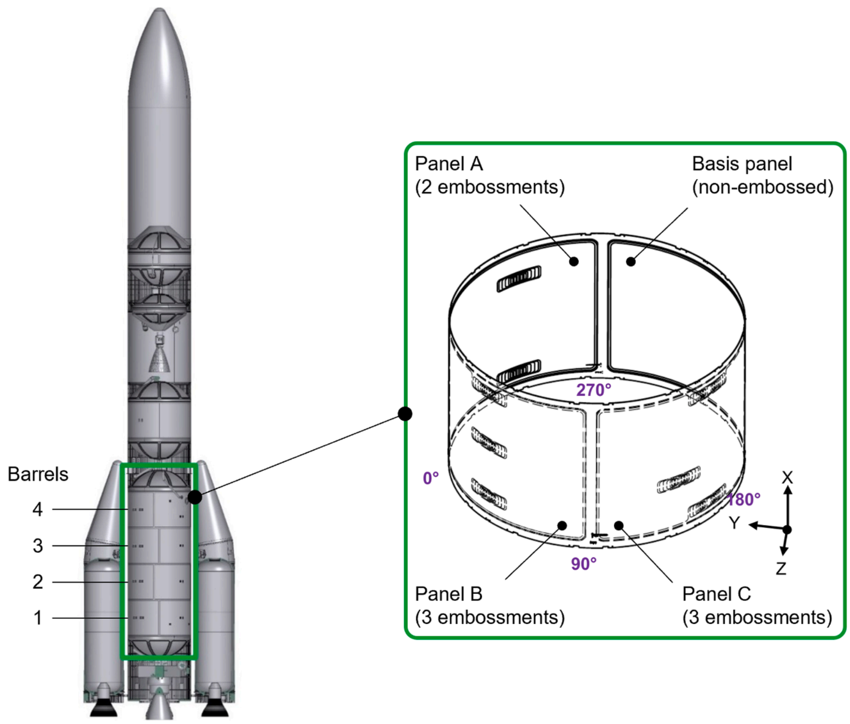


**Fig. 3.** Position of the LLPM LH2 tank barrel segments in Ariane 6 (left) and schematic of the hybrid test article (right).

shows, on the left, the position of the four cylindrical barrel segments within the Ariane 6 launch vehicle, and on the right, a schematic view of the described hybrid test article. For confidentiality reasons, further details of the tested barrel segment and its local reinforcements are not disclosed.

Mechanical material properties, i.e., Young's modulus $E$, Poisson's ratio $\nu$, and density $\rho$ are obtained from the MMPDS [48] and are summarized in Table 1 (values refer to room temperature conditions).

**Table 1**
Mechanical properties of AA2219-T87 aluminum alloy at room temperature [48].

| $E$ [GPa] | $\nu$ | $\rho$ [kg/m$^3$] |
|---|---|---|
| 70 | 0.33 | 2,823 |

## 2.2. Load cases

IMA Dresden developed the test rig, specimen interfaces, and loading concept to meet the required load distribution, under the authority of MTA. Fig. 4 provides a schematic overview of the experimental setup, explicitly illustrating the structural components, load introduction paths, and boundary conditions. The specimen is positioned between the upper and lower support frames and is radially constrained via specimen support rings mounted on both frames. Four hydraulic actuators are arranged circumferentially and introduce the load into the upper support frame. The load is transferred to the specimen through the support interfaces, where a shim layer is introduced after specimen mounting to homogenize the contact conditions and mitigate local stress concentrations.

The support frames are robust steel structures designed to be significantly stiffer than the test specimen, such that their deformation is negligible in comparison. Their geometry, including height, is defined by the requirements of the actuator system, load introduction paths, and instrumentation layout, ensuring proper load transfer without influencing the global structural response of the barrel. Detailed design information is not available due to proprietary constraints. The configuration shown in Fig. 4 allows controlled superposition of axial and bending loads, as well as mass compensation for the upper support frame, without the need to modify the actuator configuration. The actuator layout and the investigated circumferential region are illustrated in Fig. 5. The four hydraulic actuators are positioned at the center of each panel, while the highlighted sector defines the primary area of interest for the experimental evaluation.

The loading was applied using one primary actuator operating in synchronization with replica actuators, all operating simultaneously during the test. Fig. 6 shows a detailed view of one actuator installed within the test article, highlighting the main components of the load introduction system, namely the hydraulic actuator, the load cell, and the upper support frame.

The primary actuator was operated in pure displacement control, with force feedback measured and used as input to the control loops of the replica actuators. The replica actuators were controlled via virtual force control loops, relying on the factored force feedback from the primary hydraulic actuator. To ensure stable operation during buckling events, an internal cascading displacement feedback loop was added to each replica actuator's force control loop. This cascade functioned similarly to pure displacement control but was initiated by a force-based input. Fig. 7 presents a diagram of the control loop strategy for a single replica actuator.

The study involved two load cases that subjected the structure to different bending configurations. Table 2 summarizes the relative load applied to each actuator, as defined by MTA during the qualification test planning, with the objective of validating modeling and assessment approaches rather than reproducing a one-to-one operational condition. In Load Case 1 (LC1), three actuators applied the load while the fourth remained in a mass-compensated state (i.e., applying the corresponding portion of the mass from the upper support frame). Actuator 4 was displacement-driven, whereas Actuators 1 and 3 maintained a normalized load ratio of 0.898 relative to the main actuator. The aim of the test configuration was to induce elastic buckling in Panel C (see Fig. 5). In Load Case 2 (LC2), only Actuators 1 and 4 were active, with the re-

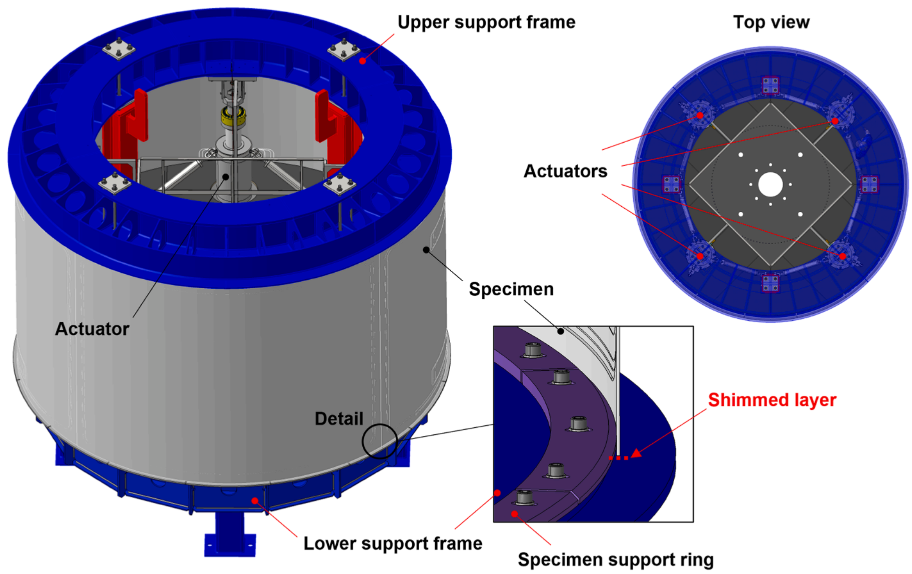


**Fig. 4.** Schematic overview of the test rig developed by IMA Dresden, showing the main structural components, load introduction system, and boundary conditions applied to the specimen.

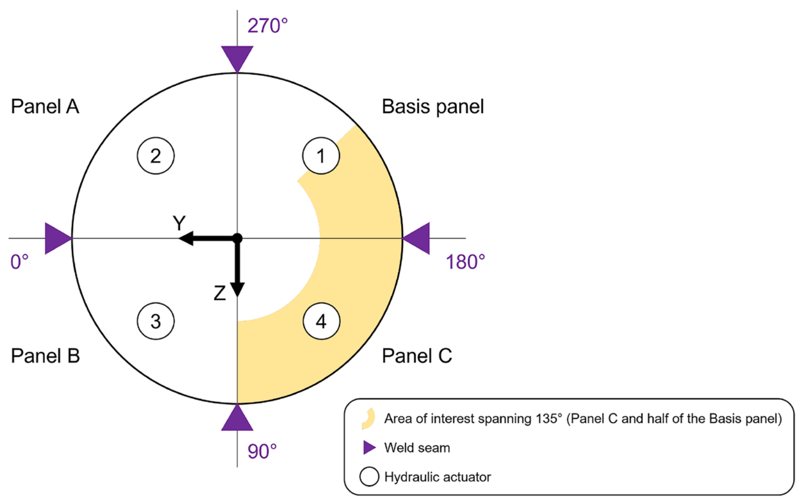


**Fig. 5.** Schematic representation of the four hydraulic actuators and the area of interest of the test specimen.

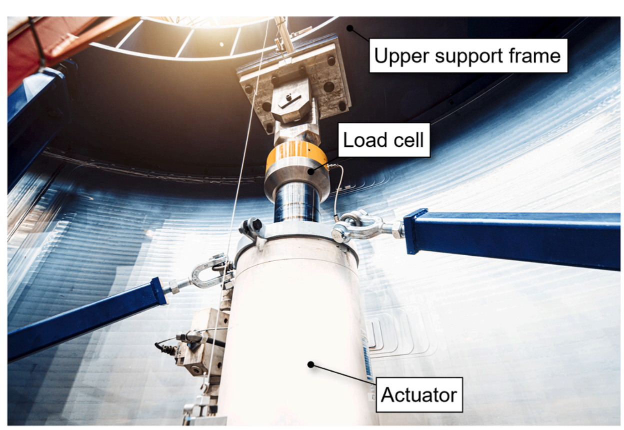


**Fig. 6.** Detail of the hydraulic actuator system installed within the test article, showing the actuator, load cell, and upper support frame.

maining two in a mass-compensated state. As in LC1, Actuator 4 was displacement-driven, while the second active actuator applied the same force. This configuration introduced a combined axial–bending loading state, promoting a localized instability at the weld seam between the Basis panel and Panel C (see Fig. 5), where increased imperfection sensitivity and stress concentration are expected. Such loading conditions are representative of non-uniform load distributions that may arise in realistic structural configurations and are therefore relevant for assess-

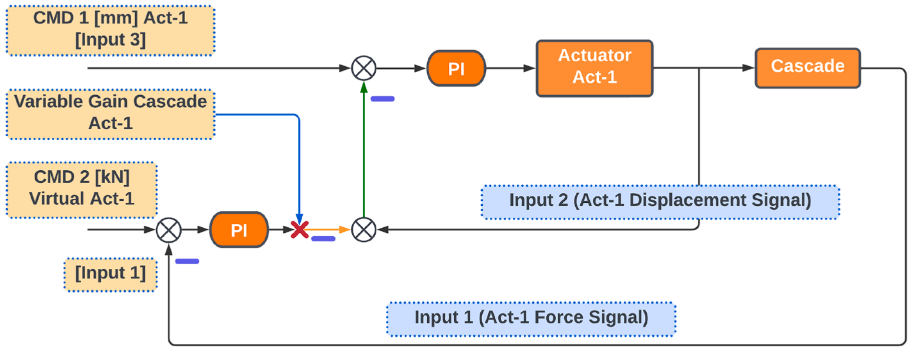


**Fig. 7.** Control loop strategy for a replica actuator developed by IMA Dresden.

ing the structural response under combined loading. Since no fixed connection existed between the upper support frame and the tank section, separation between these components could not be fully prevented, particularly on the side opposite to the buckling location.

**Table 2**
Definition of the load cases, including actuator positions and normalized load ratios.

| Load case | Actuator | Circumferential position [°] | Normalized load ratio |
|---|---|---|---|
| 1 | 1 | 225 | 0.898 |
| | 2 | 315 | 0 |
| | 3 | 45 | 0.898 |
| | 4 | 135 | 1 |
| 2 | 1 | 225 | 1 |
| | 2 | 315 | 0 |
| | 3 | 45 | 0 |
| | 4 | 135 | 1 |

Based on the normalized loads listed in Table 2 and using the coordinate system defined in Fig. 5, the resulting axial and bending load components were calculated, considering that the actuators are positioned at a radial distance of 2 m from the origin (as specified by MTA). The results are presented in Table 3.

**Table 3**
Resultant axial and bending load components for each load case.

| Load case | $F_x$ | $F_y$ | $F_z$ | $M_x$ | $M_y$ | $M_z$ |
|---|---|---|---|---|---|---|
| 1 | −2.796 | 0 | 0 | 0 | $-\sqrt{2}$ | $-\sqrt{2}$ |
| 2 | −2 | 0 | 0 | 0 | 0 | $-2\sqrt{2}$ |

These axial and bending components highlight the primary differences between LC1 and LC2. In LC1, a diagonal bending pattern (with an absolute magnitude of 2) is superimposed on a stronger axial load, promoting a more uniform compressive deformation over Panel C. In contrast, LC2 features a lower axial component but dominant unidirectional bending about the $z$-axis, which may trigger different imperfection sensitivities or asymmetric buckling modes—particularly along the weld seam between the Basis and C panels.

The loading profiles for both load cases were established by prescribing the loading conditions, step sequences, ramps, and hold times. VCT measurements were conducted at selected load steps—first in the mass-compensated state and subsequently always below the buckling load predicted by the nonlinear FE analysis (see Section 3.2). Additionally, higher static preload steps were taken into account for VCT loading steps beyond 58.4% of the predicted buckling load for LC1 and 55.9% for LC2. These intermediate preload levels were introduced to ensure stable measurement conditions during the VCT acquisition. Since VCT was not the primary objective of the experimental campaign, the loading sequence was defined to avoid unintended buckling during frequency measurements, which could be triggered by load fluctuations or actuator control deviations near the critical load. For this purpose, the structure was temporarily loaded to higher levels and subsequently unloaded to the target VCT step, where the vibration measurements were performed.

Fig. 8(a) shows the planned loading scheme for Actuator 4 for LC1, and Fig. 8(b) presents the corresponding chart for LC2, both in terms of the 20th percentile of the nonlinear buckling loads calculated in Section 3.2, here denoted $P_{\mathrm{NL,\,20\%}}$. It is important to emphasize that this nonlinear buckling analysis does not represent design values, but rather a scientific estimation conducted specifically for this study. These values are employed in the figures to maintain consistency within this paper, although they were not originally used to plan the experimental campaign.

The loading profiles, as shown in Fig. 8, differ between the cases. This modification was made specifically for LC2, which was expected to involve plastic deformation. Note that the relative load levels appear high because, for consistency within this paper, the load sequence is expressed in terms of the nonlinear buckling load ($P_{\mathrm{NL,\,20\%}}$) calculated in this study. Furthermore, it should be emphasized that this was not a dedicated VCT experiment, and was therefore not designed to be non-destructive.

To clarify the control approaches for the load cases, and following the actuator positions given in Fig. 5, Fig. 9 specifies the control strategy implemented for each hydraulic actuator in LC1 and LC2.

## 3. Finite element model

The FE model was originally built on Nastran by MTA and subsequently redefined in Abaqus by DLR/PFH as part of this research project. As a result, the herein defined FE model yields research-only results and is not official, nor used for sizing primary structural components of Ariane 6.

### 3.1. Overview of the FE model

The cylindrical barrel is discretized on its outer surface using linear quadrilateral thin-shell elements (Abaqus S4R). A total of 1172 shell elements are used along the circumference, providing sufficient resolution to capture the buckling, vibration, and imperfection-sensitivity characteristics of the test article. Multiple shell sections are assigned throughout the barrel to accurately represent padups, local reinforcements, and other geometric design features. Nonlinear static analyses are performed using the Newton–Raphson iterative procedure with artificial damping stabilization, whereas the Lanczos eigensolver is employed for the linear buckling and free-vibration computations. A schematic view of the FE model, highlighting the different shell sections as well as the MPC-based coupling between the barrel and the test rig superelements, is provided in Fig. 10. This representation allows capturing the compliance of the

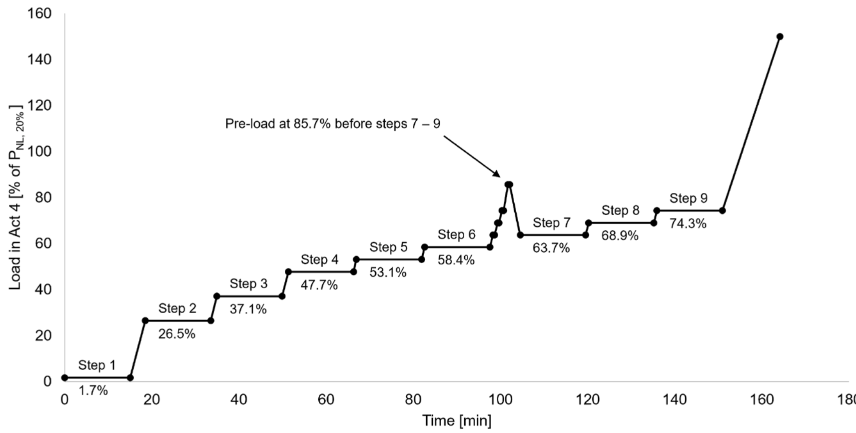


(a) LC1.

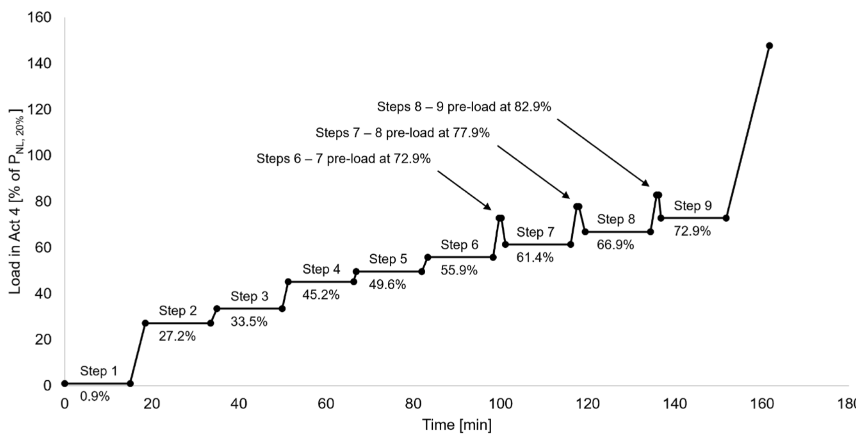


(b) LC2.

**Fig. 8.** Planned loading schemes for actuator 4 in load cases LC1 (a) and LC2 (b), shown in terms of the 20th percentile of the nonlinear buckling loads ($P_{NL,\,20\%}$).

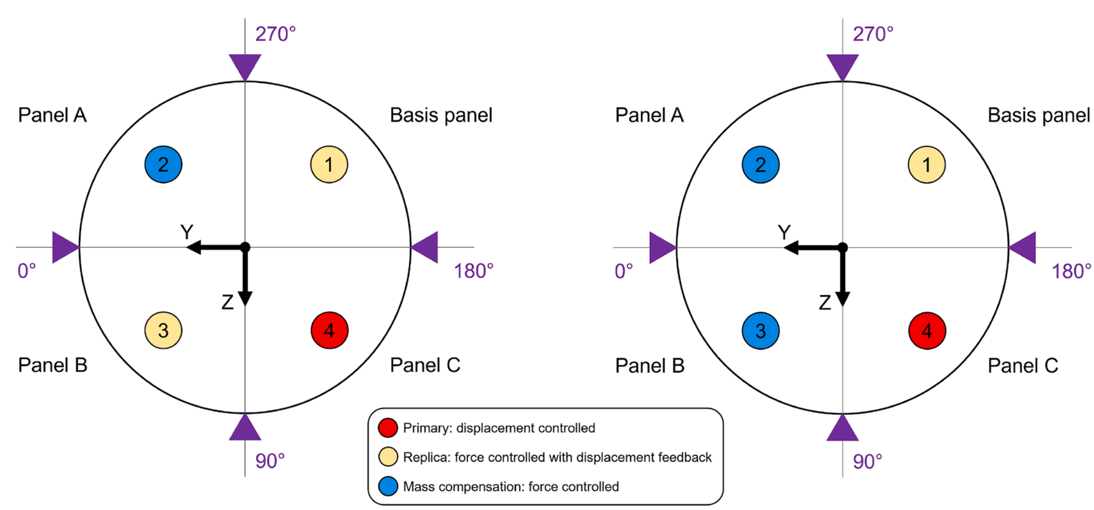


(a) LC1. (b) LC2.

**Fig. 9.** Schematics of the actuator control strategies implemented for LC1 (a) and LC2 (b).

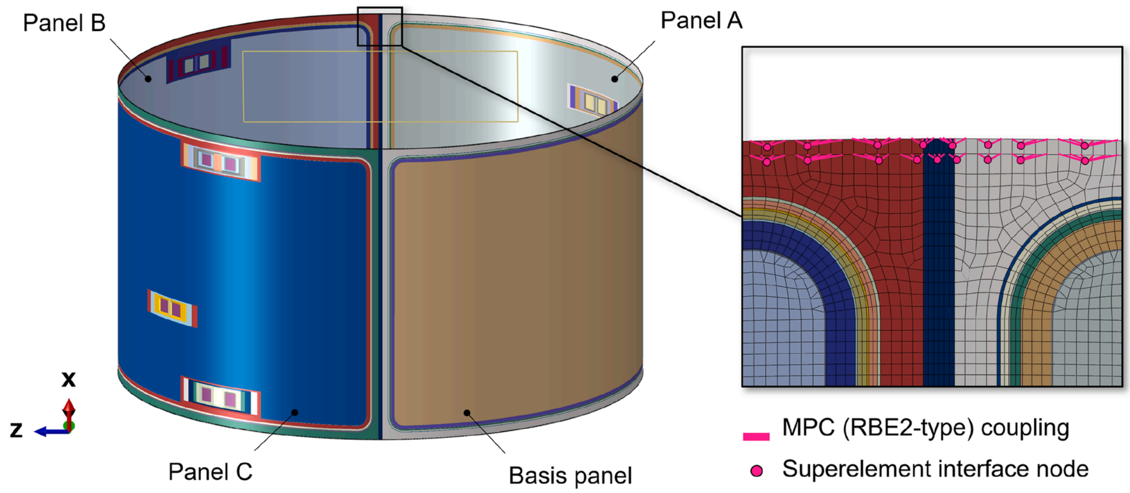


**Fig. 10.** FE model of the test article showing the shell section distribution (colored) and the coupling to the test rig via MPC (RBE2-type) constraints at the superelement interface (detail view).

support frames, which would be otherwise neglected in simplified rigid or tie-based boundary conditions.

The test rig is represented through two superelements corresponding to the lower and upper support frames. Both were originally supplied by MTA in Nastran punch file format and subsequently converted to Abaqus for inclusion as user-defined elements. These superelements provide a reduced-order representation of the test fixture, preserving its global stiffness characteristics and load transfer behavior.

- The lower superelement consists of 768 structural nodes, 4 actuator-interface nodes, and 1 control node. The control node is located at the global origin and receives the general boundary conditions of the model.
- The upper superelement consists of 634 structural nodes and 4 actuator-interface nodes.

In total, these 1402 superelement nodes are connected to the upper and lower edges of the barrel through multi-point constraint equations (MPCs), ensuring displacement compatibility and allowing a realistic representation of the interaction between the shell structure and the test rig, as schematically represented in Fig. 4.

For reproducing the actuators and control loop of the replica actuators, linear constraint equations and the Abaqus user-defined amplitude (UAMP) subroutine are utilized. For each pair of actuator interfaces (upper and lower), a control node coincident with the lower interface node is defined. This node receives the enforced displacement or applied load (depending on the actuator) and distributes it kinematically to the upper and lower interfaces through the following linear constraint equation:

$$u_{\mathrm{DOF}}^{\mathrm{UPPER}} - u_{\mathrm{DOF}}^{\mathrm{CONTROL}} - u_{\mathrm{DOF}}^{\mathrm{LOWER}} = 0 \qquad (6)$$

which is enforced for the three translational degrees of freedom. This formulation ensures that the actuator force is distributed according to the relative stiffnesses of the upper and lower interfaces, thereby accurately reproducing the real test conditions. Fig. 11 illustrates, on the left, the upper and lower superelements with the actuator-interface nodes, and on the right the actuator representation based on the control and interface nodes. For clarity, the control node is shown slightly offset from the lower interface node.

Concerning the control loop, the force-feedback configuration shown in Fig. 7 is reproduced in the FE simulation by means of a UAMP subroutine. In the analysis, an enforced displacement is prescribed at the primary actuator's control node, which is monitored as a sensor within the Abaqus quasi-static step. The reaction force at this node is measured at the beginning of each increment and used to calculate the load applied to the replica actuators through the UAMP subroutine. This load amplitude is applied directly to the control nodes of the active replica actuators. By updating the replica actuator loads in proportion to the measured reaction force at the primary actuator, this approach maintains the load ratios defined in Table 2 throughout the simulation, including in the post-buckling regime—and prevents overshoot in the applied loads. The main characteristics of the FE model are summarized in Table 4.

**Table 4**
Main characteristics of the FE model.

| Solver | Standard |
|---|---|
| Shell element type | S3R/S4R |
| Number of nodes | 266,290 |
| Number of elements | 263,818 |
| Nodes in superelements | 1411 |

As expected, the outer surface deviation was measured; nevertheless, its disclosure is not included in the present research agreement. Therefore, the nonlinear static solution considers a pristine model and two types of mid-surface imperfection patterns:

1. the first linear buckling mode (LB1, see Fig. 13), used as a single-mode imperfection,
2. two imperfection patterns obtained by multiplying a Fourier-based pattern by a stochastic perturbation field (see Fig. 12).

The amplitude of these imperfection patterns is defined as a percentage of the nominal thickness: 50%, 100%, and 200% for (1), and 50%, 100%, 200%, 300%, and 400% for (2).

An example of Fourier-based imperfection patterns can be found in [49]. In the present study, a similar approach is devised, consisting of identifying an imperfection pattern from the DLR database through the Fourier series and then scaling the reconstructed pattern using a stochastic perturbation field. The original measured imperfection field used in this process originates from an unrelated industrial project and cannot be disclosed; however, the methodology for generating stochastic, Fourier-based imperfections is fully presented here, together with representative examples. A key advantage of this method lies in the synergy between the continuous character of experimentally measured imperfections and the smooth basis functions of the Fourier series, which together ensure realistic and topologically consistent synthetic imperfection patterns. The Fourier series in its trigonometric form [50] can be expressed

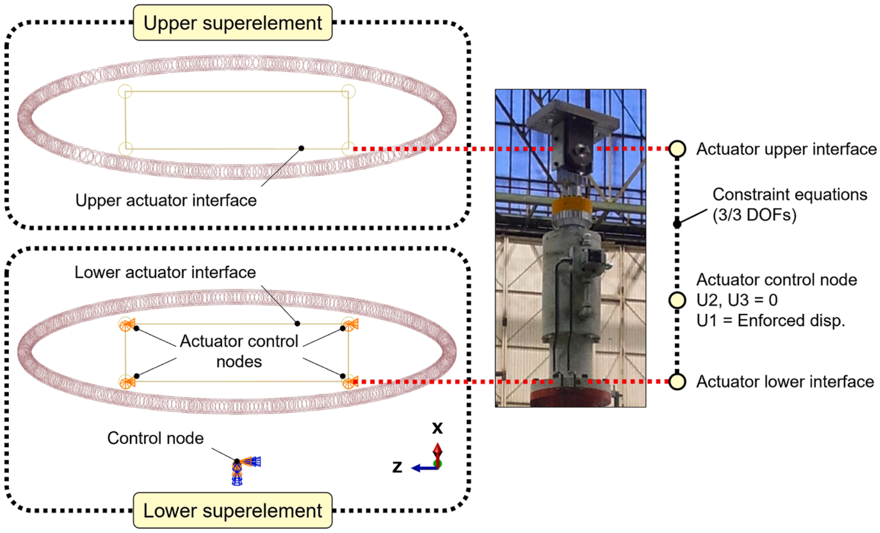


**Fig. 11.** Finite-element representation of the support-frame superelements (left) and actuator modeling approach (right).

in the $(x, \theta)$-coordinates as:

$$f(x,\theta) = \sum_{m,n=1}^{\infty} \left[A_{mn}\cos(m\pi x)\cos(n\theta) + B_{mn}\sin(m\pi x)\cos(n\theta) + \right.$$
$$\left. + C_{mn}\cos(m\pi x)\sin(n\theta) + D_{mn}\sin(m\pi x)\sin(n\theta)\right] \tag{7}$$

where $m$, $n$ stand for the number of meridional and circumferential harmonics, $A_{mn}$, $B_{mn}$, $C_{mn}$, $D_{mn}$ for the Fourier coefficients, $x$ and $\theta$ for the meridional and circumferential normalized coordinates varying from 0 to 1 and $-\pi$ to $\pi$, respectively. The Fourier coefficients are calculated through the integral equations [50] (also presented here in $(x, \theta)$-coordinates):

$$A_{mn} = \int_0^1 \int_{-\pi}^{\pi} f(x,\theta)\cos(m\pi x)\cos(n\theta)dxd\theta$$
$$B_{mn} = \int_0^1 \int_{-\pi}^{\pi} f(x,\theta)\sin(m\pi x)\cos(n\theta)dxd\theta$$
$$C_{mn} = \int_0^1 \int_{-\pi}^{\pi} f(x,\theta)\cos(m\pi x)\sin(n\theta)dxd\theta$$
$$D_{mn} = \int_0^1 \int_{-\pi}^{\pi} f(x,\theta)\sin(m\pi x)\sin(n\theta)dxd\theta \tag{8}$$

The least-squares solution is used for computing the Fourier coefficients for a given imperfection pattern. To devise the random imperfection patterns, the identified coefficients are multiplied by a random vector $\bar{e}$, which in turn is calculated as:

$$\bar{e} = \left((e - \min(e))\frac{2}{\max(e) - \min(e)} - 1\right)\left(\frac{A_{\mathrm{NOISE}}}{100}\right) + 1 \tag{9}$$

where $e$ is a vector whose length equals the number of identified Fourier coefficients, and contains random numbers generated from a univariate normal (Gaussian) distribution with zero mean and unit variance. Note that $\bar{e}$ is a normalized version of $e$ that fluctuates within a desired noise amplitude $A_{\mathrm{NOISE}}$. For example, if $A_{\mathrm{NOISE}}$ is set to 25%, the random normalized vector $\bar{e}$ has random amplitudes distributed between 0.75 and 1.25. After multiplying the Fourier coefficients by $\bar{e}$, the amplitude of the imperfection pattern can be scaled to the desired magnitude.

In this paper, the detailed FE model aims to accurately represent the buckling behavior of a launch-vehicle-like barrel structure and to provide insight into its structural response beyond the critical load. In addition, the model is used to corroborate the definition of the VCT load steps previously introduced in Fig. 8. Therefore, the described random-Fourier-based methodology is employed to generate two imperfection patterns, depicted in Fig. 12. As noted before, the reference imperfection field from the DLR database originates from an unrelated industrial project and cannot be disclosed; however, the methodology is illustrated through these two representative patterns generated through the above-described process. The first pattern (a) resembles four weld seam lines consistent with TIG-induced HAZ and the associated local deviations of our specimen, while the second pattern (b) introduces broader disturbances in the shell geometry featuring multiple waves in both axial and circumferential directions, superimposed on pattern (a). As previously mentioned, each pattern will be scaled by 50%, 100%, 200%, 300%, and 400% of the nominal thickness—while the charts themselves are scaled to the full barrel length and 100% of the nominal thickness—, resulting in ten FE analyses per load case.

The imperfection patterns illustrated in Fig. 12 will hereafter be referred to as Fourier Mid-Surface Imperfections (FMSI). Employing FMSI enables a systematic assessment of the effects of realistic imperfections on structural response, thereby improving the stability assessment.

### 3.2. Numerical results

Firstly, the model is solved for the linear buckling load, necessary for evaluating the VCT in situ during the test campaigns. To achieve this, unit loads following the ratios defined for the load cases in Table 2 are applied to loaded actuators. Additionally, the LB1 was used as stress-free mid-surface imperfection pattern for the nonlinear solution described below. Fig. 13 shows the first five linear buckling modes for the evaluated load cases, together with the corresponding $P_{\mathrm{CR}}$ for the primary actuator $P_{\mathrm{CR,\,ACT\text{-}4}}$.

The results in Fig. 13 corroborate the expected buckling mode shapes for load cases in which the compressive load is not applied uniformly along the structural edges, leading to the concentration of buckling waves in regions of higher compressive stress. Moreover, the first buckling mode captures the dominant local instability shape relevant for the loading configurations investigated here, making it representative for the imperfection studies and subsequent nonlinear analyses.

A modal analysis was also performed, determining the frequency range of interest for the vibration tests. The eigenvalue problem was solved for the first 50 vibration modes. Fig. 14 shows Modes 1, 23, 28, 45, and 48, providing representative examples of the modal shapes expected during the experimental campaign.

As shown in Fig. 14, the vibration modes of interest are in a frequency range between 20 and 60 Hz. Furthermore, the results indicate that measuring an arc length encompassing three half-waves of the first vibration mode is sufficient to distinguish Mode 48—provided that a

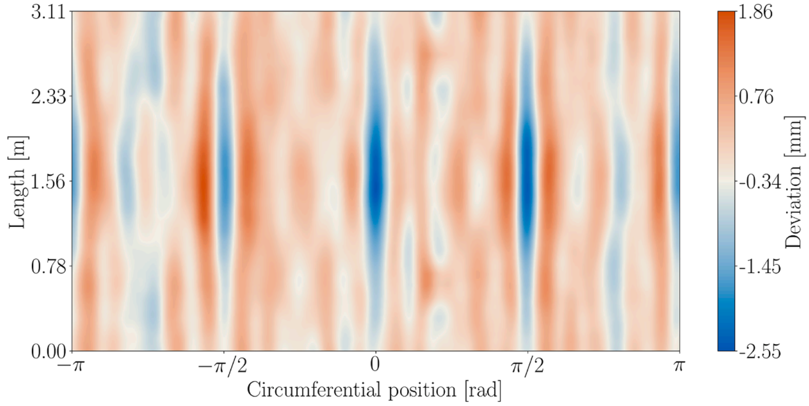


(a) Fourier imperfection signature disturbing the welding seam locations (FMSI1).

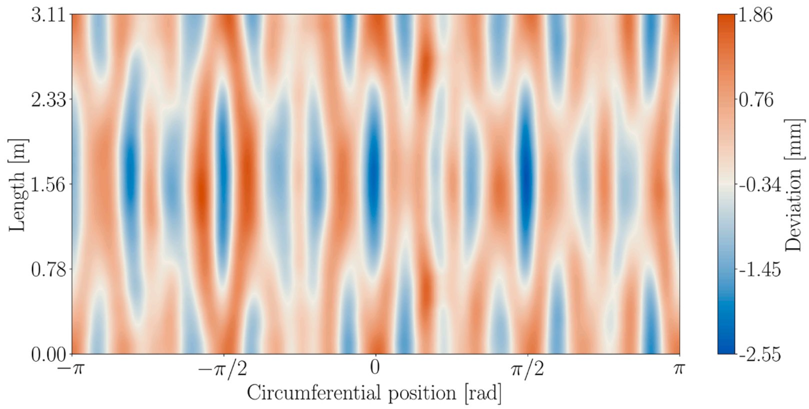


(b) Fourier imperfection signature disturbing the whole structure (FMSI2).

**Fig. 12.** Random Fourier imperfection patterns: (a) signature disturbing the welding seam locations (FMSI1), (b) signature disturbing the whole structure (FMSI2).

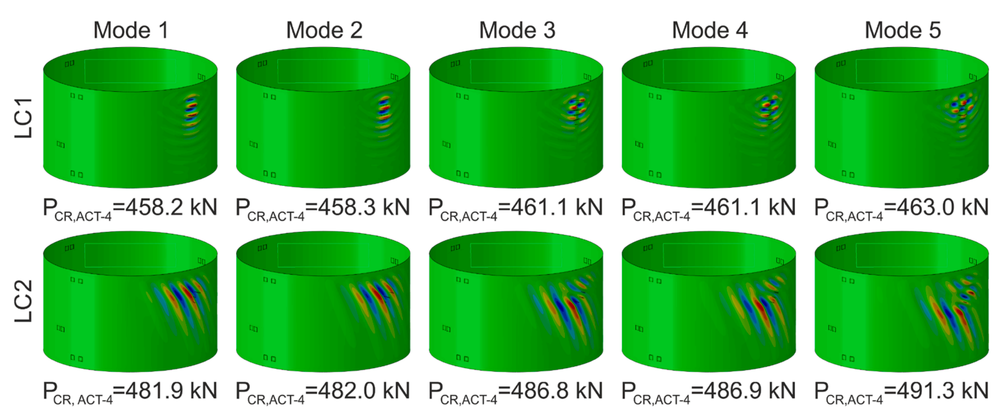


**Fig. 13.** First five linear buckling modes for LC1 (top row) and LC2 (bottom row).

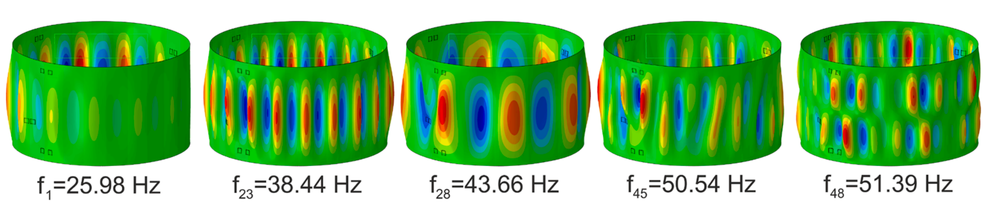


**Fig. 14.** Selected vibration modes of the unloaded barrel, illustrating representative modal shapes.

sufficiently fine measurement grid is used. This corresponds to a minimum arc length of approximately 45°, or one-third of the area of interest defined in Fig. 5.

The nonlinear FE results are evaluated in terms of the primary actuator displacement, see Fig. 9, and its corresponding reaction force. Fig. 15 presents these curves for both load cases and all imperfection

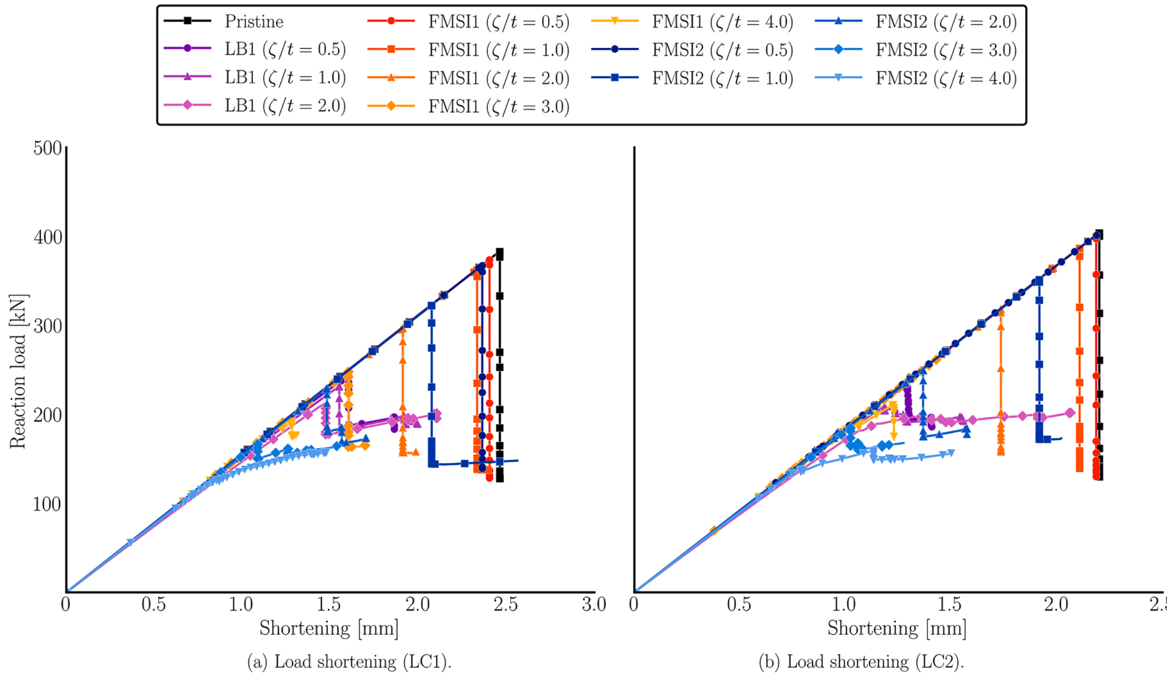


**Fig. 15.** Numerical nonlinear static load–shortening results for the primary actuator: (a) LC1; (b) LC2.

patterns considered, and Table 5 provides the corresponding maximum load-bearing capacity and numerical knockdown factor $\gamma_{\mathrm{NL}}$ calculated as the ratio between nonlinear and linear buckling loads.

**Table 5**
Numerical load-bearing capacities and nonlinear knockdown factors ($\gamma_{\mathrm{NL}}$) for all imperfection cases in LC1 and LC2.

| ID | Model | $P_{\mathrm{NL,\,ACT\text{-}4,\,LC1}}$ [kN] | $P_{\mathrm{NL,\,ACT\text{-}4,\,LC2}}$ [kN] | $\gamma_{\mathrm{NL,\,LC1}}$ | $\gamma_{\mathrm{NL,\,LC2}}$ |
|---|---|---|---|---|---|
| 1 | Pristine | 382.51 | 403.53 | 0.83 | 0.88 |
| 2 | LB1 ($\zeta/t = 0.5$) | 243.30 | 230.05 | 0.53 | 0.50 |
| 3 | LB1 ($\zeta/t = 1.0$) | 231.15 | 208.56 | 0.50 | 0.46 |
| 4 | LB1 ($\zeta/t = 2.0$) | 212.06 | 201.93 | 0.46 | 0.44 |
| 5 | FMSI1 ($\zeta/t = 0.5$) | 373.45 | 401.66 | 0.82 | 0.88 |
| 6 | FMSI1 ($\zeta/t = 1.0$) | 362.31 | 386.43 | 0.79 | 0.84 |
| 7 | FMSI1 ($\zeta/t = 2.0$) | 296.70 | 317.86 | 0.65 | 0.69 |
| 8 | FMSI1 ($\zeta/t = 3.0$) | 247.90 | 261.36 | 0.54 | 0.57 |
| 9 | FMSI1 ($\zeta/t = 4.0$) | 191.53 | 210.65 | 0.42 | 0.46 |
| 10 | FMSI2 ($\zeta/t = 0.5$) | 366.92 | 400.96 | 0.80 | 0.88 |
| 11 | FMSI2 ($\zeta/t = 1.0$) | 322.09 | 351.18 | 0.70 | 0.77 |
| 12 | FMSI2 ($\zeta/t = 2.0$) | 228.83 | 249.25 | 0.50 | 0.54 |
| 13 | FMSI2 ($\zeta/t = 3.0$) | 166.47 | 184.64 | 0.36 | 0.40 |
| 14 | FMSI2 ($\zeta/t = 4.0$) | 157.45 | 158.96 | 0.34 | 0.35 |

Analyzing the nonlinear FE results shown in Fig. 15 and Table 5, the trends are consistent with expectations for nonlinear buckling analysis. Specifically, imperfections based on LB1 yield more conservative predictions than those obtained from FMSI, resulting in a significant reduction in load-carrying capacity even at small mid-surface imperfection magnitudes (notably for LC2 with $\zeta/t = 2.0$). In contrast, results with FMSI2 resemble the classic thin-walled cylindrical shell buckling scenario, where a sudden drop in load-carrying capacity is observed. This drop becomes more pronounced as the imperfection magnitude increases, approaching a pure-bending response at larger values (see the curves for FMSI2 with $\zeta/t = 4.0$). Additionally, the results indicate that imperfections focused only on the weld seam regions (FMSI1) may be non-conservative, as they produce higher load-carrying capacities than other cases. To consolidate these findings, Fig. 16 presents the nonlinear buckling loads for both load cases, arranged in ascending order to illustrate the influence of imperfection pattern and amplitude. The color scheme from Fig. 15 and the model IDs from Table 5 are retained for consistency.

The load-bearing capacities, arranged in ascending order, indicate that the imperfections based on LB1 are the most critical, providing a more conservative assessment of the structure for identical $\zeta/t$ values. Notably, even at the smallest imperfection magnitude ($\zeta/t = 0.5$), the corresponding load-bearing capacities fall within the upper half of the results—ranking as the 8th and 9th most critical for LC1 and LC2, respectively. For both load cases, the lowest capacities are observed for FMSI2 with $\zeta/t$ ratios of 3.0 and 4.0.

To provide a quantitative reference for the experimental results, the buckling load corresponding to the 20th percentile of the simulated nonlinear results is highlighted. The corresponding values—199.74 kN ($\gamma_{\mathrm{NL}} = 0.44$) for LC1 and 204.58 kN ($\gamma_{\mathrm{NL}} = 0.42$) for LC2—represent the threshold below which 20% of the numerically predicted buckling capacities fall. The experimental buckling load remains below this 20th-percentile reference, indicating that even when adopting a conservative lower-bound percentile, the numerical model still tends to overestimate the capacity. It should be noted that potential local stiffness reductions associated with TIG-induced HAZ are not explicitly represented in the numerical model; this may partially explain the discrepancy between numerical predictions and experimental results. Overall, this behavior emphasizes the significant influence of uncertainties inherent in imperfection-sensitive structures and the variability observed in experimental conditions. For a more comprehensive treatment of imperfection sensitivity in shell structures, including the role of measured geometric imperfections and boundary condition effects within a probabilistic context, the reader is referred to Wagner et al. [51], who develop a mechanistic design approach. In their work, the classical definition of the KDF [19] is reformulated in terms of the Batdorf parameter $Z$, thereby incorporating the combined influence of slenderness and shell length into the analysis. This representation enables the identification of distinct stability regimes governed by different dominant triggers, namely global imperfections, interaction effects, and localized instabilities. Within this approach, these regimes are systematically analyzed and formalized through a mechanistic design curve, providing a structured interpretation of imperfection sensitivity across a wide range of shell configurations.

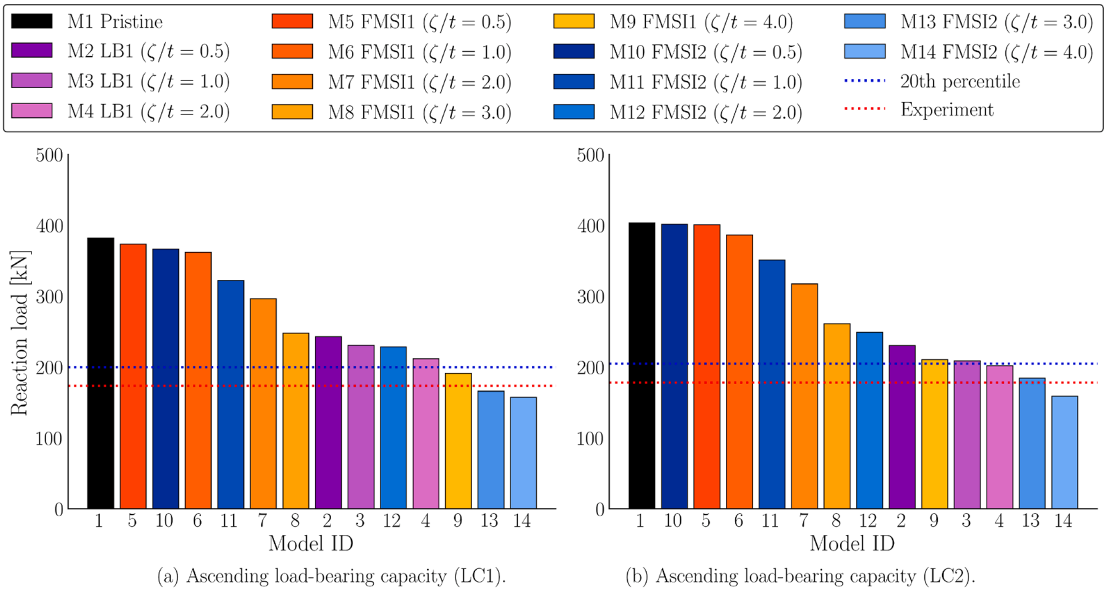


**Fig. 16.** Nonlinear buckling loads for (a) LC1 and (b) LC2, arranged in ascending order. Colors and model IDs follow Fig. 15 and Table 5: M1 Pristine; M2–M4 LB1 ($\zeta/t = 0.5, 1.0, 2.0$); M5–M9 FMSI1 ($\zeta/t = 0.5, 1.0, 2.0, 3.0, 4.0$); M10–M14 FMSI2 ($\zeta/t = 0.5, 1.0, 2.0, 3.0, 4.0$).

Additionally, the FE models are employed to numerically investigate the VCT methodology. Specifically, the nonlinear results obtained using meshes disturbed by LB1 and FMSI2 with $\zeta/t = 2.0$ are divided into 10 equally spaced load steps, up to 90% of the corresponding $P_{\mathrm{NL}}$, with a linear frequency step included after each load step. The variation of the first three vibration modes with respect to the applied load is evaluated to assess the expected accuracy of VCT during the experimental campaign, as proposed in [29,52]. Fig. 17 shows: (a) and (c) the characteristic curves, and (b) and (d) the VCT relative difference $\delta$ with respect to the corresponding nonlinear buckling load for the first three vibration modes under LC1 and LC2, respectively. The quality of the quadratic fits used to construct the VCT characteristic curves is assessed via the coefficient of determination $R^2$, which is consistently reported in the legends of all VCT characteristic charts to quantify the goodness-of-fit.

The selection of $\zeta/t = 2.0$ for both LB1 and FMSI2 is based on a representative intermediate imperfection level defined a priori, rather than on agreement with the experimental results. The objective is to demonstrate the VCT methodology under realistic, non-calibrated conditions and to assess its robustness across plausible imperfection scenarios.

The consistently high $R^2$ values observed confirm that the quadratic approximation provides an adequate representation of the structural response for the considered modes and load cases. This is particularly relevant, as the VCT buckling load prediction is derived from the minimum of these fitted curves. The VCT prediction error behaves as expected, generally decreasing as the maximum load level used for estimation increases, regardless of vibration mode and load case—with the exception of Mode 3 for LC2, where a higher deviation is observed at 90% of $P_{\mathrm{NL}}$. Regarding the imperfection pattern, results for FMSI2 exhibit greater dispersion across vibration modes for both load cases, whereas for LB1 the differences between modes are less pronounced. There is a slight difference between the deviation curves for the two load cases; specifically, LC2 is associated with steeper curves, indicating that the VCT applicability for this load case is more sensitive to the maximum load step. This suggests a relationship between the deviation of the VCT prediction and the ratio of bending to compressive load for this barrel structure. In summary, the results suggest that error intervals of approximately −25% to −5% can be expected for experimental tests with measurements up to around 75% of the buckling load, for both load cases.

## 4. Experimental campaign

This section outlines the test procedures and control loop, followed by a description of the VCT measurement setup. The test results are then presented and discussed in the final subsection.

### 4.1. Test procedures and VCT measurement system

To ensure proper contact between the load introduction surfaces and the barrel edges, existing gaps between the test rig and the barrel were shimmed using aluminum shims. These shims were chosen for their stiffness properties, which are similar to those of the tested article. Circumferentially positioned strain gauges were employed to quantify the influence of this process on the barrel's response, verifying the overall effectiveness of the shimming procedure. However, these measurements are out of the scope of this research agreement. As a result of this process, the final axial gaps between the loading surfaces and the barrel section were reduced to less than 0.1 mm.

The MTS Aero ST control system, together with AeroPro software, was used to implement the control loop shown in Fig. 7, ensuring uniform load distribution along the barrel's circumference for the specified load cases. In the event of buckling or any unintended global or local overload conditions, the system automatically adjusts the load distribution to preserve the barrel's structural integrity. This is accomplished by continuously monitoring the barrel's response in real-time, preventing the load from exceeding predefined limits, which reduces the risk of failure due to excessive loading during the test.

Before each test, the hydraulic system was activated to reach stable operating conditions, minimizing thermal effects on actuator response. A mass compensation procedure was then performed to account for the dead weight of the upper support frame and loading interfaces, ensuring a mechanically neutral initial state. This reference condition was recorded by all measurement systems, including the VCT setup, to provide a consistent baseline for the subsequent tests.

The VCT test setup includes a loudspeaker used to excite the barrel and a laser vibrometer that scans its surface to measure vibration velocity. The loudspeaker (Yamaha HS7 studio monitor) is mounted close to the lower exterior side of the barrel, maintaining a gap of approximately 10–20 mm. The position was chosen to be as close as possible to the

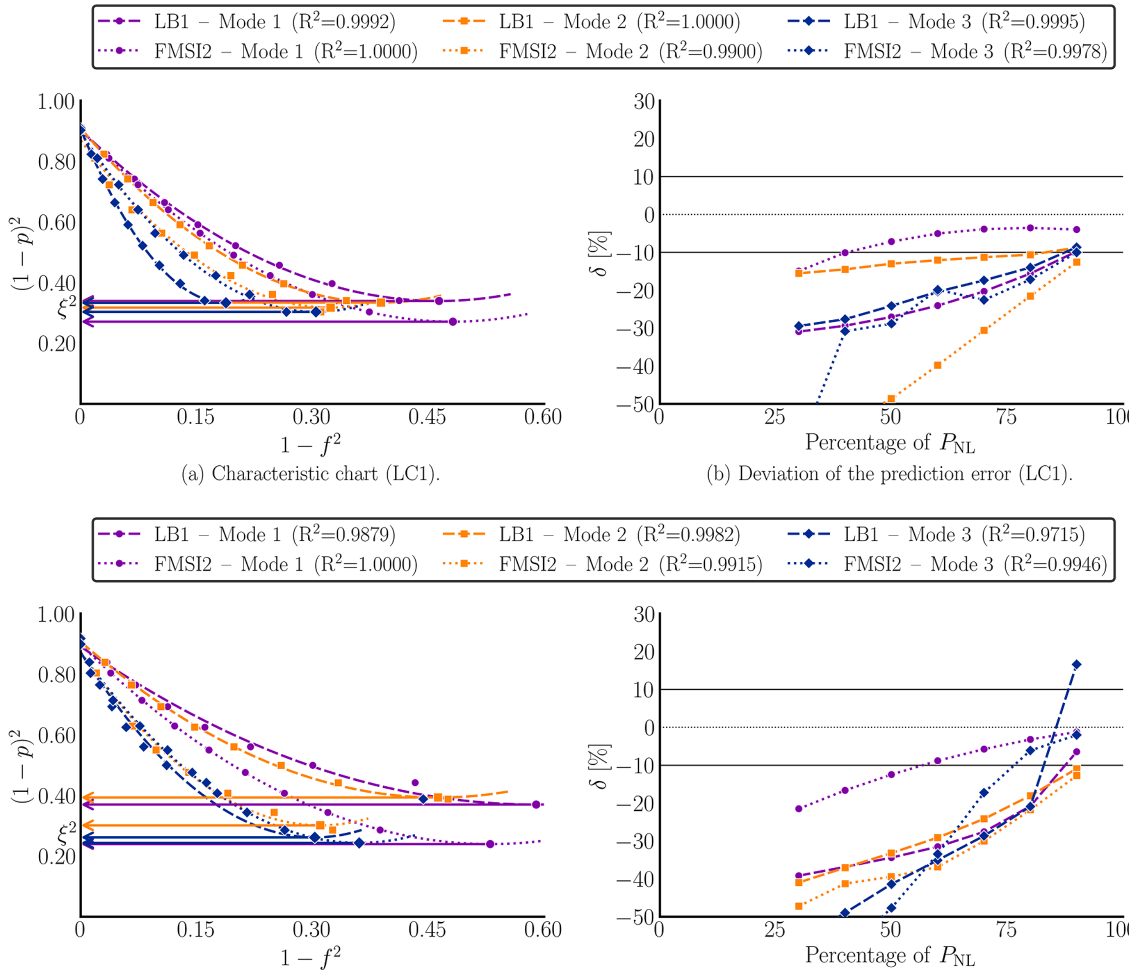

(a) Characteristic chart (LC1). (b) Deviation of the prediction error (LC1).
(c) Characteristic chart (LC2). (d) Deviation of the prediction error (LC2).

**Fig. 17.** Characteristic charts and prediction-error deviations for numerical models with LB1 and FMSI2 imperfections ($\zeta/t = 2.0$): (a), (c) characteristic charts for LC1 and LC2; (b), (d) corresponding prediction-error deviations.

scanned region, ensuring sufficient excitation while avoiding interference with the DIC system. The excitation signal consists of a chirp input covering the frequency range of interest (4–250 Hz), enabling a broadband characterization of the structural response. In practice, effective excitation is achieved within the operational bandwidth of the loudspeaker, and preliminary vibration measurements confirmed that the relevant global modes of the structure were sufficiently excited, yielding clean and repeatable modal shapes suitable for VCT analysis.

The laser vibrometer used is the Polytec PSV400 2D, positioned approximately 8 m from the barrel. The Polytec workstation for data acquisition and post-processing is located near the scanner. Two measurement grids were defined according to the load case. For LC1, the surface was scanned using a grid of 10 × 8 points, whereas for LC2 a grid of 7 × 9 points was used. The laser vibrometer measures the velocity at each of these points, covering the section of the cylindrical shell that is also monitored by the digital image correlation (DIC) system during the buckling experiment. The measurement grids were defined based on the expected modal content from preliminary FE analysis (see Fig. 14)), providing sufficient spatial resolution to capture the dominant half-wave patterns in the region of interest. The grid density was chosen to enable clear identification of modal shapes, while maintaining a manageable number of measurement points for repeatable acquisition across load steps. This configuration provides a good compromise between measurement time and reliable mode tracking for VCT analysis.

For illustration, Fig. 18(a–c) presents the experimental arrangement for LC2, the scanning laser vibrometer, and the loudspeaker used during the VCT test campaign, while Fig. 18(d) provides a schematic representation of the subsequent modal parameter identification process.

To assess the modal parameters of the structure, each vibration test involved exciting the cylindrical shell using the loudspeaker shown in Fig. 18(c). The resulting vibration velocity was measured at all points of the specified grids for LC1 and LC2, and the modal analysis was performed using Polytec software. Measurements were taken over a frequency range of 0–60 Hz with 480 spectral lines for the first experiment, and 0–100 Hz with 1000 spectral lines for the second experiment, yielding frequency resolutions of 0.125 Hz and 0.1 Hz, respectively. This adjustment in frequency resolution was made after evaluating the results of the first experiment, where a higher resolution would have provided better discrimination of the vibration modes. As a result, a less dense mesh was used for the second experiment, helping to maintain a nearly unchanged measurement time.

### 4.2. Experimental results for LC1

In LC1 experimental campaign, buckling occurred at a total load of 485.1 kN. The buckling load magnitude was made available for the present study as a reference for the VCT predictions, while no additional data (e.g., load–shortening response) were included in the dataset. This corresponds to 86.8% of the buckling load assumed as the 20th percentile of the numerical results (558.5 kN for the total applied load). Consequently, the load sequence portrayed in Fig. 8(a) was influenced and the actual load ratios for the VCT steps are 2%, 30.5%, 42.7%,

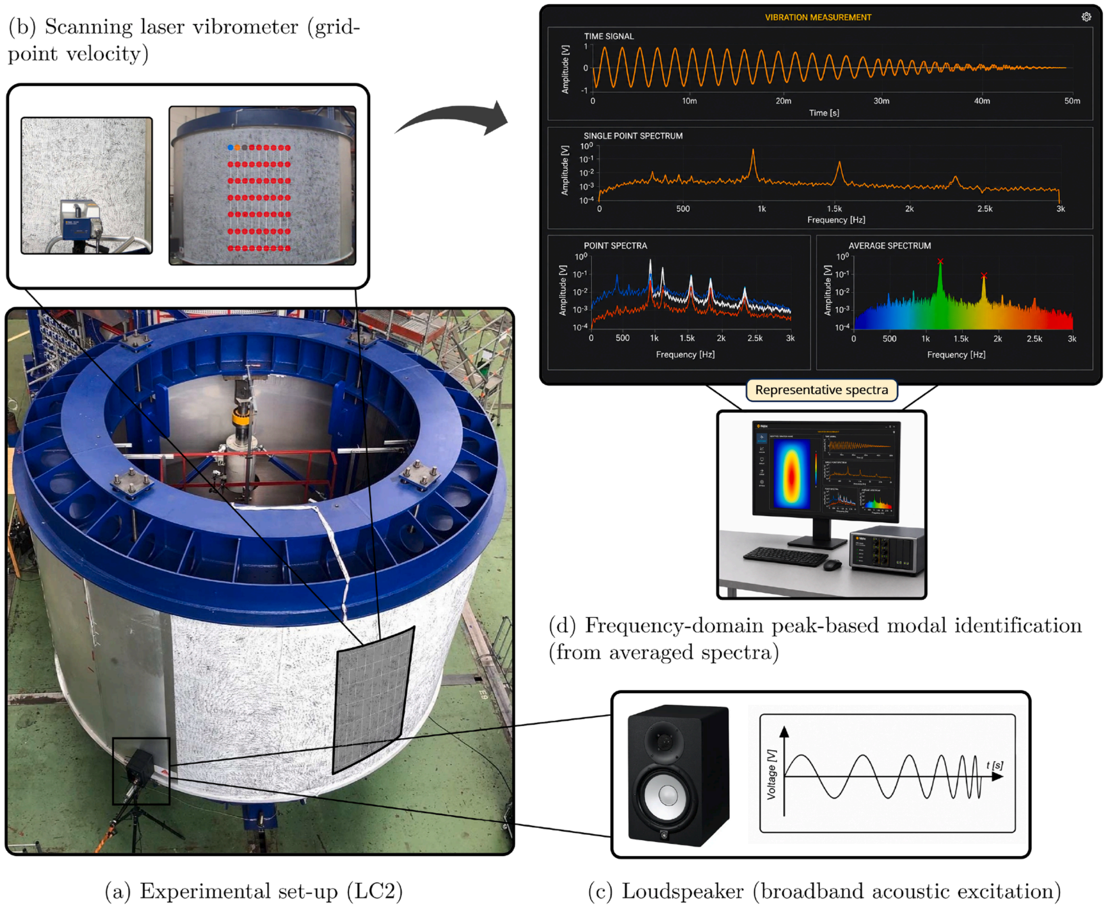


**Fig. 18.** Schematic overview of the VCT test setup for LC2: (a) experimental arrangement, (b) Polytec scanning laser vibrometer, (c) loudspeaker for acoustic excitation, and (d) schematic modal parameter identification process (FFT and estimator).

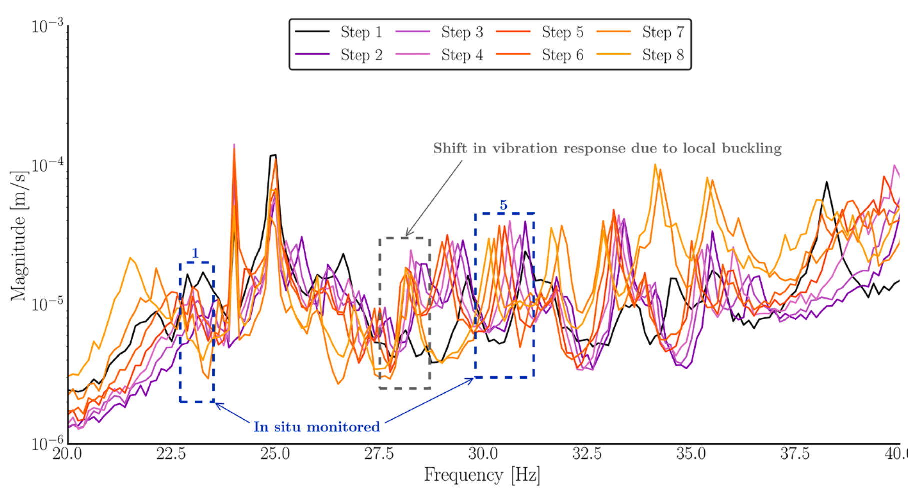


**Fig. 19.** Average vibration spectra for each VCT load step in LC1, highlighting in situ monitored vibration modes and modal shifts due to local buckling.

54.9%, 61.1%, 67.2%, 73.3%, 79.4%, and 85.5% of the experimental buckling load. Furthermore, the pre-load, which was originally set at 85.7%, corresponded to 98.7% of the experimental buckling load.

A local buckling event occurred during the pre-load phase planned in Fig. 8(a), at a load ratio corresponding to 80.7% of the experimental buckling load, thereby affecting the last three VCT load steps. The occurrence of local buckling is clearly identified in the structural vibration response through the observed shifts in modal characteristics. Fig. 19 shows the experimentally measured average spectra for each VCT load step, highlighting the in situ monitored vibration modes and the shift in modal characteristics following the local buckling phenomenon.

It is noteworthy that, following the occurrence of local buckling between load steps 6 and 7, certain vibration modes either disappeared or exhibited significant changes in amplitude. This effect is particularly evident when comparing the vibration modes for consecutive load steps. As an example, Fig. 20 presents the experimentally measured evolution of Modes 1 and 5 as a function of the applied load. These two modes were tracked in situ because their corresponding vibration responses

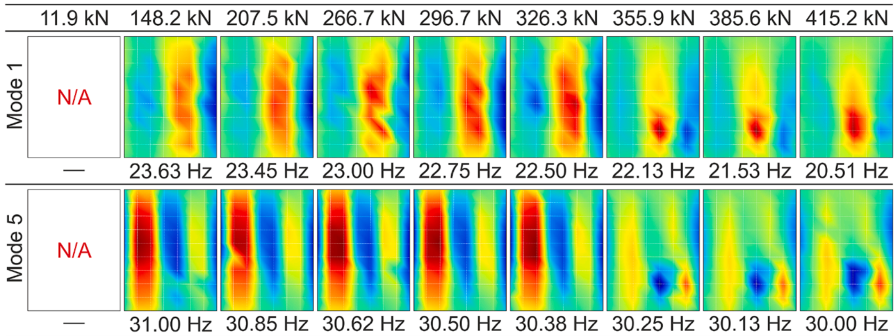


**Fig. 20.** Experimentally measured evolution of modes 1 and 5 (monitored in situ) with applied load over the VCT steps in LC1.

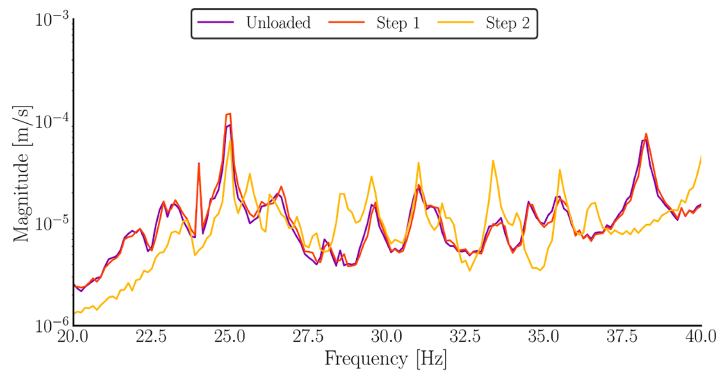


**Fig. 21.** Average spectra for the unloaded condition and first two VCT load steps in LC1.

exhibited the highest measurement quality and showed a consistent frequency evolution throughout LC1. It should be noted, however, that they could not be clearly identified at the first load step.

In Fig. 20, the pronounced influence of local buckling on the vibration response is clearly visible, as the amplitude of the central circumferential half-wave of the first and fifth vibration modes are significantly affected in the last three VCT load steps. Furthermore, Fig. 19 reveals two persistent signals at 24 Hz and 25 Hz, which are attributed to interference from external equipment—particularly the 25 Hz signal, which corresponds to half the frequency of the power supply. Unfortunately, these interference signals overlap with the frequency range of the first vibration modes (as predicted by the FE analysis, see Fig. 14), thereby hindering their use for VCT-based buckling load predictions.

Inconsistencies are observed in the frequency response of the structure, particularly during the initial VCT measurement, when the structure was in a mass-compensated state. Fig. 21 compares the frequency response in the unloaded state (used for equipment calibration) with those measured during the first two VCT load steps.

Fig. 21 demonstrates that the frequency response of the structure in the unloaded state closely matches that observed during the first VCT load step (mass-compensated state), but deviates significantly at the second VCT load step. This inconsistency is reflected in the appearance of new vibration modes during the second load step and in the absence of a distinct frequency drop between the first two VCT measurements. Additionally, the figure highlights that the measurement resolution of 0.125 Hz is not sufficiently refined, as some frequency peaks are not well defined.

Regarding the VCT evaluation, Fig. 22(a) presents the quadratic fits for Modes 1 and 5, considering all available load steps. Fig. 22(b) shows the variation of the prediction error $\delta$ with respect to the load step (expressed in terms of $P_{\mathrm{EXP,\,LC1}}$). As expected, the minimum of the quadratic fit decreases when measurements at higher load ratios are included, resulting in a smaller prediction error as the load step approaches $P_{\mathrm{EXP,\,LC1}}$.

The high $R^2$ values indicate a very good agreement between the quadratic fits and the measured data, confirming that the assumed functional form adequately represents the VCT characteristic curves. The results presented in Fig. 22 were obtained in situ, with Mode 5 yielding the most accurate buckling load predictions, showing deviations of $-5.6\%$ and $4.3\%$ for load steps up to 79.4% and 85.5% of $P_{\mathrm{EXP,\,LC1}}$, respectively. In comparison, the deviations for Mode 1 at these load steps were $-20.9\%$ and $-14.8\%$. Subsequent post-test analysis of the measured data confirmed that the best buckling load predictions for LC1 were obtained using the fifth vibration mode.

### *4.3. Experimental results for LC2*

Similarly to LC1, buckling in LC2 occurred earlier than predicted, with global buckling observed at 356 kN, which corresponds to approximately 87% of the FE prediction (409.2 kN). As in LC1, only the buckling load magnitude was made available for the present study as a reference for the VCT predictions, without additional data. A local buckling event was detected at 345 kN, representing 97% of the global buckling load. Considering the measured global buckling load, the load ratios depicted in Fig. 8(b) were adjusted to approximately 1%, 31.3%, 38.5%, 51.9%, 57%, 64.2%, 70.6%, 76.9%, and 83.8% of the experimental buckling load. Fig. 23 presents the frequency response of the structure for LC2, shown as the average spectra for each VCT load step, with emphasis on the in situ monitored vibration modes (Modes 2 and 12).

Discrepancies are evident in the structural frequency response for LC2, particularly when comparing the initial VCT load steps (steps 1 and 2) to the subsequent ones. Notably, new vibration modes emerge during step 2, without a smooth transition from step 1. As for LC1, a detailed post-test assessment of additional vibration mode candidates was conducted to ensure the best possible VCT predictions. Fig. 24 illustrates the experimentally measured evolution of Modes 2 and 22 across the load steps. Mode 2 was tracked in situ during testing due to the high quality of its recorded vibration response and consistent frequency evolution,

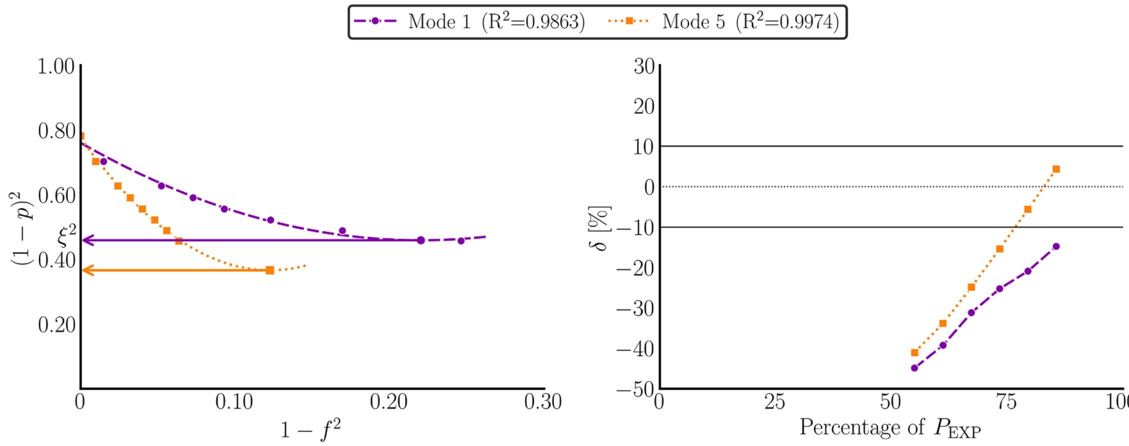


(a) Characteristic chart (LC1). (b) Deviation of the prediction error (LC1).

**Fig. 22.** VCT analysis for LC1: (a) quadratic fits for Modes 1 and 5; (b) corresponding prediction error $\delta$ versus load step.

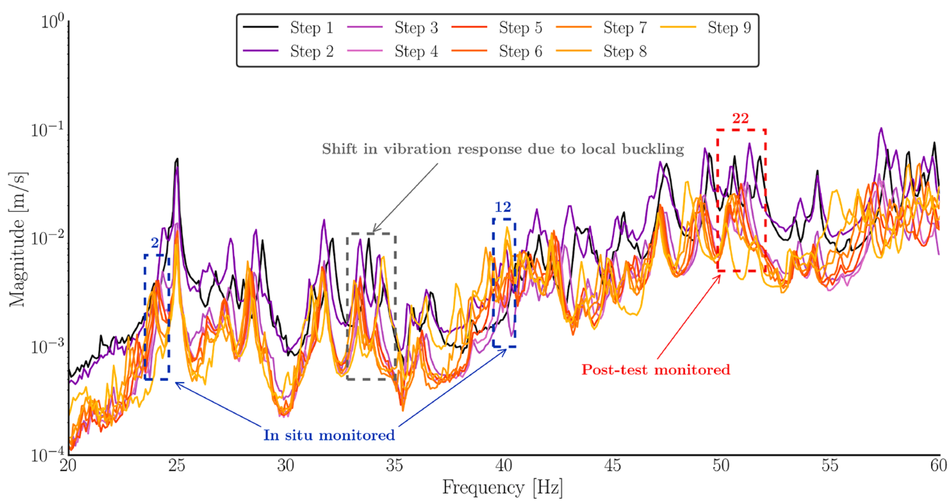


**Fig. 23.** Average vibration spectra for each VCT load step in LC2, highlighting in situ and post-test monitored vibration modes and modal shifts due to local buckling.

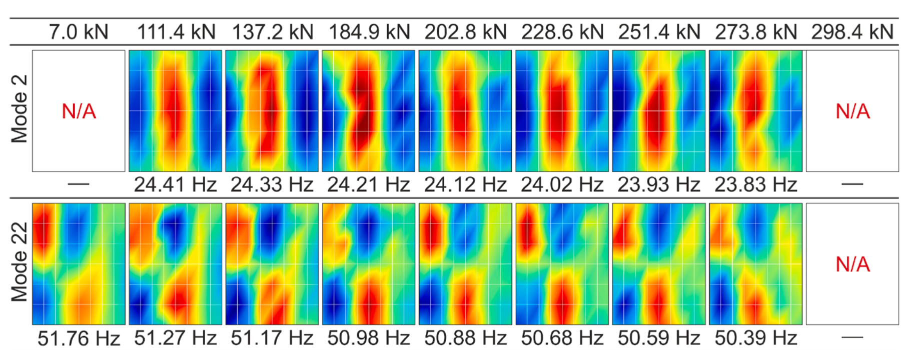


**Fig. 24.** Experimentally measured evolution of Modes 2 (monitored in situ) and 22 (identified post-test) with applied load over the VCT steps in LC2.

whereas Mode 22 was identified only during post-test evaluation. It is observed that Mode 2 could not be identified in the first and last VCT load steps, while Mode 22 was already present in the first load step and was therefore evaluated as an additional candidate for VCT prediction.

This figure also demonstrates that the alternative preloading strategy adopted for LC2 (see Section 4.1) resulted in experimental measurements free from interference by buckling phenomena up to the final load ratio. Finally, Fig. 25(a) shows the VCT characteristic chart for the measured load steps, considering both in situ and post-test evaluated vibration modes. For consistency, the analysis is limited to load steps between 111.4 kN and 273.8 kN. Fig. 25(b) presents the corresponding prediction errors $\delta$ with respect to $P_{\text{EXP, LC2}}$.

The results confirm that the methodology provides reliable buckling load predictions for LC2, with deviations of −12.9%, −23.8%, and −20.1% at 76.9% of $P_{\text{EXP, LC2}}$ for Modes 2, 12, and 22, respectively. Once again, the high $R^2$ values confirm the robustness of the quadratic approximation used to derive the VCT predictions. These findings are consistent with the FE predictions, which indicated that LC2 is more sensitive to the maximum load ratio; the prediction error decreases more rapidly with increasing load ratio for LC2 than for LC1, as anticipated by the

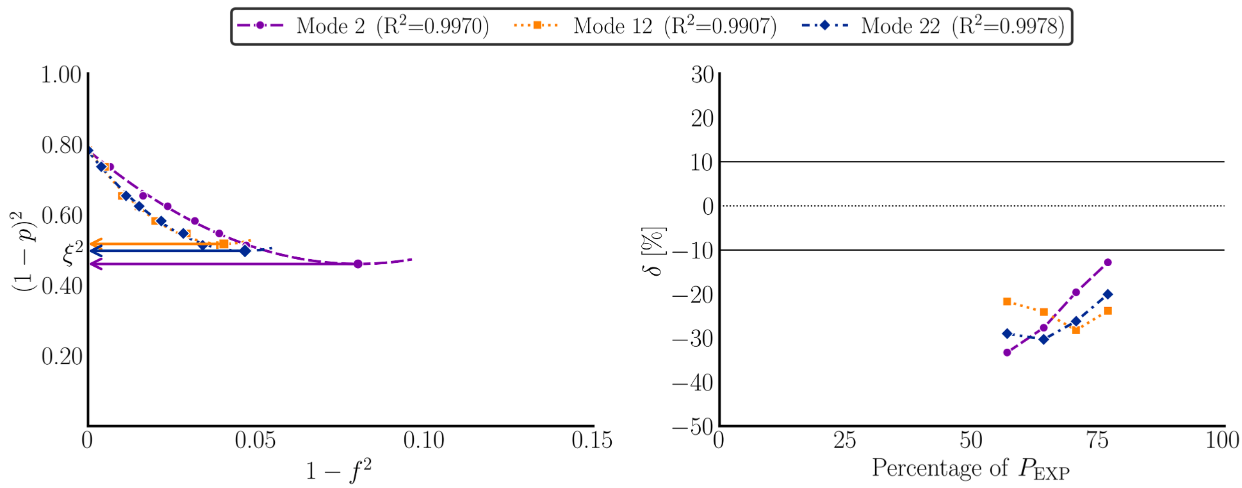

(a) Characteristic chart (LC2). (b) Deviation of the prediction error (LC2).

**Fig. 25.** VCT analysis for LC2: (a) quadratic fits for Modes 2, 12, and 22; (b) corresponding prediction error $\delta$ versus load step.

FE analysis. As with LC1, post-test investigations did not identify additional modes that would improve VCT prediction. Nevertheless, Mode 22 is included to demonstrate the methodology's accuracy for higher-order vibration modes.

## 5. Final remarks

This work presents an experimental and numerical investigation of the VCT for predicting buckling loads in a full-scale launcher barrel representative of the Ariane 6 lower stage hydrogen tank. The structure was tested under two combined axial–bending load cases, enabling assessment of the method under qualification-relevant conditions.

### 5.1. Main conclusions

The principal contributions of this study are summarized as follows:

1. *Experimental validation of VCT for full-scale shells:* The VCT methodology, previously validated for downscaled specimens [23–30], was successfully applied to a full-scale metallic barrel under qualification-relevant boundary and loading conditions, providing reliable, in situ buckling load predictions. For both load cases, appropriate vibration modes were identified and tracked in situ through multiple load steps. The resulting buckling load predictions showed deviations of −5.6% and 4.3% for LC1 (Mode 5), while remaining conservative for LC2 (Mode 2) with a deviation of −12.9%. To the authors' knowledge, this constitutes the first experimental validation of VCT at full scale within a launcher qualification campaign.
2. *Performance under combined loading conditions:* The experimental campaign demonstrated that VCT remains applicable under combined axial–bending loading and multi-actuator configurations representative of qualification conditions. For LC1, VCT predictions were more accurate at intermediate load steps but became non-conservative at the highest measured load. In LC2, which involved a different actuator configuration, the technique remained robust and conservative, but the predictions were more sensitive to maximum load step. Overall, the results confirm the applicability of VCT to complex multi-actuator loading configurations, demonstrating its robustness beyond idealized laboratory conditions.
3. *Numerical analysis and imperfection sensitivity:* A detailed FE framework was developed, combining nonlinear analysis with imperfection descriptions based on both classical linear buckling modes and stochastic Fourier-based representations. This approach enabled a systematic evaluation of imperfection sensitivity and knockdown factors. The results demonstrate that stochastic descriptions provide a broader representation of imperfection variability, while linear buckling-mode-based imperfections establish a conservative baseline for structural assessment.
4. *Implications for qualification and design verification processes:* The integration of VCT demonstrates a promising path forward for non-destructive verification within structural qualification tests of imperfection-sensitive aerospace structures. The methodology enables early, in situ estimation of buckling loads, reducing the need for destructive testing and offering potential savings in time and cost. Furthermore, this work introduces a novel framework for imperfection modeling that extends classical Fourier-based formulations into a stochastic approach, enabling the generation of representative imperfection fields from limited measurement data. When integrated with detailed FE analysis, this method provides a practical means to quantify imperfection sensitivity and supports the structural assessment of full-scale structures, for which such measured imperfection data are typically scarce.

### 5.2. Critical assessment

Despite the overall consistency of the results, several factors limit the predictive accuracy of the proposed methodology and should be considered when interpreting the outcomes. Importantly, these limitations do not undermine the experimental validation of VCT presented in this study, but rather define the range of conditions under which the obtained predictions should be regarded as reliable.

1. *Experimental limitations:* Since the VCT prediction is obtained from the extrapolation of the Arbelo characteristic curve rather than from a direct measurement at the critical state, the maximum load ratio reached during testing directly affects the conditioning of the prediction. Measurements performed too far from the critical-load range may still provide smooth characteristic trends, but they increase the sensitivity of the inferred buckling load to curve fitting, frequency resolution, and mode selection. Increasing proximity to the critical load improves the robustness of the extrapolation but is constrained by test safety and operational limits. Higher frequency resolution enhances the stability of the identified characteristic curves, yet requires longer acquisition times at each load step, introducing a trade-off between measurement accuracy and test efficiency. Moreover, high coefficients of determination for the quadratic fits should be regarded as a necessary but not sufficient condition for reliable prediction, since the physical relevance of the selected vibration mode

remains equally important. Dedicated vibration-focused test campaigns would allow improved control of these parameters and potentially enhance prediction accuracy.

2. *Numerical modeling limitations:* The numerical results depend strongly on the representation of geometric imperfections, material properties, and boundary conditions. In the absence of measured imperfection fields, stochastic Fourier-based descriptions and linear buckling modes were adopted to provide a broad and statistically representative range of imperfection patterns. Although this approach provides a rational substitute for unavailable measurement data, it cannot fully replace direct geometric characterization of the tested structure. This approach improves coverage compared to deterministic assumptions; nevertheless, it does not guarantee inclusion of the most critical imperfection configuration governing the structural response. In addition, local stiffness reductions associated with the TIG-induced HAZ are not explicitly represented. While these effects may be partially reflected in the adopted imperfection shapes, localized material degradation and stiffness heterogeneities at the weld seams are not directly included in the model. Furthermore, simplified representations of support conditions and interface behavior, such as the omission of shimming effects, introduce additional uncertainty in the predicted response. Consequently, the numerical results should be interpreted as a physically informed reference framework rather than as a unique deterministic representation of the tested barrel.
3. *Experimental data availability:* The validation of the numerical models is inherently limited by the availability of experimental data within the research agreement. In particular, load-shortening curves and detailed post-buckling response were not accessible. Access to such data would enable a more comprehensive validation of the numerical models, extending beyond buckling load predictions to the full nonlinear structural response. This would also allow a more direct assessment of whether discrepancies between numerical and experimental VCT predictions originate primarily from modal identification, boundary-condition idealization, imperfection modeling, or global nonlinear response.
4. *Experimental system uncertainties:* Additional variability arises from the experimental setup, including load introduction imperfections and actuator synchronization. These factors may lead to non-ideal load distributions and local deviations from the intended boundary conditions, influencing both the measured structural response and the identification of representative vibration modes. Their combined effect contributes to the observed scatter and represents an inherent limitation of full-scale testing under complex multi-actuator configurations. Such uncertainties are particularly relevant for qualification-scale structures, for which the test setup itself may become an inseparable part of the measured structural response.

Overall, the present results should be interpreted as a validation of the applicability of VCT to full-scale launcher structures under qualification-relevant conditions, rather than as a fully deterministic prediction framework independent of test and modelling assumptions. While the methodology proves robust and applicable at full scale, its predictive capability remains dependent on three coupled factors: the maximum experimentally achievable load ratio, the robustness of modal identification and tracking, and the fidelity with which boundary conditions, actuator synchronization, and geometric imperfections are represented. Further improvements are expected through higher achievable load levels during testing, dedicated vibration measurement strategies, direct characterization of geometric imperfections, and refined modelling of boundary and interface conditions.

## CRediT authorship contribution statement

**Felipe Franzoni:** Writing – review & editing, Writing – original draft, Visualization, Validation, Supervision, Software, Methodology, Investigation, Formal analysis, Data curation, Conceptualization; **Theodor Dan Baciu:** Writing – review & editing, Methodology, Investigation, Data curation, Conceptualization; **Richard Degenhardt:** Writing – review & editing, Resources, Project administration, Methodology, Investigation, Funding acquisition, Data curation, Conceptualization; **Adrian Gliszczyński:** Writing – review & editing, Visualization, Project administration, Methodology, Investigation, Data curation, Conceptualization; **Klaus Stromer:** Resources, Project administration, Investigation; **Jens Hornschuh:** Writing – review & editing, Validation, Resources, Investigation, Conceptualization; **Kaspars Kalnins:** Validation, Resources, Investigation, Conceptualization; **Eduards Skukis:** Validation, Resources, Investigation, Conceptualization; **Jochen Albus:** Writing – review & editing, Supervision, Project administration, Methodology, Investigation, Data curation, Conceptualization.

## Declaration of competing interest

The authors declare that they have no known competing financial interests or personal relationships that could have appeared to influence the work reported in this paper.

## Acknowledgments

The research leading to these results has received funding from the European Community's Ninth Framework Programme under priority ERDF (European Regional Development Fund), grant agreement nos. ZW 6–85042584 and ZW 6–87006427, as well as from the Latvian Council of Science, Latvia (grant agreement no. LZP-2018/2-363). This research was also supported by the National Science Centre, Poland (grant agreement no. UMO-2024/53/B/ST8/01594). All support is gratefully acknowledged.

The authors would also like to thank ArianeGroup GmbH, MT Aerospace AG, and IMA Materialforschung und Anwendungstechnik GmbH for their valuable support and for enabling participation in the test campaign, which allowed the use of experimental data for the validation of the VCT methodology on a full-scale barrel structure.

The information in this paper reflects only the authors' views, and the European Community is not liable for any use that may be made of the information contained herein.

## Data availability

The authors do not have permission to share data.

## References

[1] J. Singer, J. Arbocz, T. Weller, Buckling Experiments: Experimental Methods in Buckling of Thin-Walled Structures, Basic Concepts, Columns, Beams and Plates, vol. 1, John Wiley & Sons, New York, NY, USA, 2002.
[2] J. Singer, J. Arbocz, T. Weller, Buckling Experiments: Experimental Methods in Buckling of Thin-Walled Structures, Shells, Built-up Structures, Composites and Additional Topics, vol. 2, John Wiley & Sons, New York, NY, USA, 2002.
[3] F. Franzoni, Predicting buckling from vibration: an analytical, numerical, and experimental verification for cylindrical shells (2020). Bremen, DE, Ph.D. Thesis, University of Bremen
[4] J. Singer, H. Abramovich, Vibration techniques for definition of practical boundary conditions in stiffened shells, AIAA J. 17 (7) (1979) 762–769.
[5] R. Radhakrishnan, Prediction of buckling strengths of cylindrical shells from their natural frequencies, Earthq. Eng. Struct. Dyn. 2 (2) (1973) 107–115.
[6] M.A. Souza, W.C. Fok, A.C. Walker, Review of experimental techniques for thin-walled structures liable to buckling: neutral and unstable buckling, Exp. Tech. 7 (9) (1983) 21–25.
[7] M.A. Arbelo, S.F.M. de Almeida, M.V. Donadon, S.R. Rett, R. Degenhardt, S.G.P. Castro, K. Kalnins, O. Ozoliņš, Vibration correlation technique for the estimation of real boundary conditions and buckling load of unstiffened plates and cylindrical shells, Thin-Walled Struct. 79 (2014) 119–128.
[8] A. Sommerfeld, Eine einfache Vorrichtung zur Veranschaulichung des Knickungsvorganges, Z. Ver. Dtsch. Ing. 49 (1905) 1320–1323.
[9] H. Lurie, Lateral vibrations as related to structural stability, J. Appl. Mech. 19 (2) (1952) 195–204.
[10] E.E. Johnson, B.F. Goldhammer, The determination of the critical load of a column or stiffened panel in compression by the vibration method, Proc. Soc. Exp. Stress Anal. 11 (1) (1953) 221–232.

[11] A.W. Leissa, Vibration of Shells (NASA SP-288), Tech. Rep., US Government Printing Office, Washington, DC, USA, 1973.
[12] L.N. Virgin, Vibration of Axially-Loaded Structures, Cambridge University Press, Cambridge, UK, 2007.
[13] H. Abramovich, The vibration correlation technique–a reliable nondestructive method to predict buckling loads of thin walled structures, Thin-Walled Struct. 159 (2020) 107308.
[14] D. Burgreen, End-fixity effect on vibration and instability, J. Eng. Mech. Div. 86 (6) (1960) 13–28.
[15] A. Chailleux, Y. Hans, G. Verchery, Experimental study of the buckling of laminated composite columns and plates, Int. J. Mech. Sci. 17 (8) (1975) 489–498.
[16] M. Chaves-Vargas, A. Dafnis, H.-G. Reimerdes, K.-U. Schröder, Modal parameter identification of a compression-loaded CFRP stiffened plate and correlation with its buckling behaviour, Prog. Aerosp. Sci. 78 (2015) 39–49.
[17] Y. Segal, Prediction of buckling load and loading conditions of stiffened shells from vibration tests (1980). M.Sc. Thesis, Israel Institute of Technology, Haifa, IL.
[18] R.H. Plaut, L.N. Virgin, Use of frequency data to predict buckling, J. Eng. Mech. 116 (10) (1990) 2330–2335.
[19] V.I. Weingarten, P. Seide, J.P. Peterson, Buckling of Thin-Walled Circular Cylinders (NASA SP-8007), Technical Report, NASA Space Vehicle Design Criteria—Structures, Washington, DC, USA, 2020.
[20] M.A. Souza, L.M.B. Assaid, A new technique for the prediction of buckling loads from nondestructive vibration tests, Exp. Mech. 31 (2) (1991) 93–97.
[21] J. Singer, Buckling Experiments on Shells: A Review of Recent Developments (Eng. Report TAE No 403), Tech. Rep., Israel Institute of Technology, Haifa, IL, 1980.
[22] H. Abramovich, D. Govich, A. Grunwald, Buckling prediction of panels using the vibration correlation technique, Prog. Aerosp. Sci. 78 (2015) 62–73.
[23] M.A. Arbelo, K. Kalnins, O. Ozolins, E. Skukis, S.G.P. Castro, R. Degenhardt, Experimental and numerical estimation of buckling load on unstiffened cylindrical shells using a vibration correlation technique, Thin-Walled Struct. 94 (2015) 273–279.
[24] K. Kalnins, M.A. Arbelo, O. Ozolins, E. Skukis, S.G.P. Castro, R. Degenhardt, Experimental nondestructive test for estimation of buckling load on unstiffened cylindrical shells using vibration correlation technique, Shock Vib. 2015 (2015) 1–8.
[25] E. Skukis, O. Ozolins, K. Kalnins, M.A. Arbelo, Experimental test for estimation of buckling load on unstiffened cylindrical shells by vibration correlation technique, Procedia Eng. 172 (2017) 1023–1030.
[26] F. Franzoni, F. Odermann, E. Labans, C. Bisagni, M.A. Arbelo, R. Degenhardt, Experimental validation of the vibration correlation technique robustness to predict buckling of unstiffened composite cylindrical shells, Compos. Struct. 224 (2019) 111107.
[27] E. Skukis, O. Ozolins, J. Andersons, K. Kalnins, M.A. Arbelo, Applicability of the vibration correlation technique for estimation of the buckling load in axial compression of cylindrical isotropic shells with and without circular cutouts, Shock Vib. 2017 (2017) 1–14.
[28] D. Shahgholian-Ghahfarokhi, G. Rahimi, Buckling load prediction of grid-stiffened composite cylindrical shells using the vibration correlation technique, Compos. Sci. Technol. 167 (2018) 470–481.
[29] F. Franzoni, F. Odermann, D. Wilckens, E. Skukis, K. Kalninš, M.A. Arbelo, R. Degenhardt, Assessing the axial buckling load of a pressurized orthotropic cylindrical shell through vibration correlation technique, Thin-Walled Struct. 137 (2019) 353–366.
[30] E. Labans, H. Abramovich, C. Bisagni, An experimental vibration-buckling investigation on classical and variable angle tow composite shells under axial compression, J. Sound Vib. 449 (2019) 315–329.
[31] F. Franzoni, J. Albus, M.A. Arbelo, R. Degenhardt, Analytical, numerical, and experimental predictions for free vibrations and buckling of pressurized orthotropic cylindrical shells, in: Proceedings of the 69th International Astronautical Congress, Bremen, DE, 2018.
[32] F. Franzoni, R. Degenhardt, J. Albus, M.A. Arbelo, Vibration correlation technique for predicting the buckling load of imperfection-sensitive isotropic cylindrical shells: an analytical and numerical verification, Thin-Walled Struct. 140 (2019) 236–247.
[33] K. Tian, L. Huang, Y. Sun, K. Du, P. Hao, B. Wang, Fast buckling load numerical prediction method for imperfect shells under axial compression based on POD and vibration correlation technique, Compos. Struct. 252 (2020) 112721.
[34] K. Tian, L. Huang, M. Yang, Y. Chen, P. Hao, B. Wang, Concurrent numerical implementation of vibration correlation technique for fast buckling load prediction of cylindrical shells under combined loading conditions, Eng. Comput. 38 (2021) 3269–3281.
[35] D. Shahgholian-Ghahfarokhi, G. Rahimi, G. Liaghat, R. Degenhardt, F. Franzoni, Buckling prediction of composite lattice sandwich cylinders (CLSC) through the vibration correlation technique (VCT): numerical assessment with experimental and analytical verification, Compos. B: Eng. 199 (2020) 108252.
[36] E. Skukis, G. Jekabsons, J. Andersons, O. Ozolins, E. Labans, K. Kalnins, Robustness of empirical vibration correlation techniques for predicting the instability of unstiffened cylindrical composite shells in axial compression, Polymers 12 (2020) 3069.
[37] A. Gliszczynski, F. Franzoni, T. Baciu, R. Degenhardt, Predictive capabilities of vibration-correlation technique applied to axially compressed CFRP truncated cones, Compos. B: Eng. 2022 (2022) 109984.
[38] M. Zarei, G.H. Rahimi, M. Hemmatnezhad, F. Pellicano, On the buckling load estimation of grid-stiffened composite conical shells using vibration correlation technique, Eur. J. Mech. - A/Solids 96 (2022) 104667.
[39] K. Tian, L. Huang, Y. Sun, L. Zhao, T. Gao, B. Wang, Combined approximation based numerical vibration correlation technique for axially loaded cylindrical shells, Eur. J. Mech. - A/Solids 93 (2022) 104553.
[40] T.D. Baciu, R. Degenhardt, F. Franzoni, A. Gliszczynski, M.A. Arbelo, S.G.P. Castro, K. Kalnins, Sensitivity analysis for buckling characterisation using the vibration correlation technique, Thin-Walled Struct. 183 (2023) 110329.
[41] T.D. Baciu, F. Franzoni, R. Degenhardt, K. Kalnins, C. Bisagni, Shape and loading imperfection sensitivity of the vibration-correlation technique for buckling analysis of cylindrical shells, Eng. Struct. 304 (2024) 117605.
[42] T.D. Baciu, F. Franzoni, R. Degenhardt, A. Gliszczynski, C. Bisagni, Vibration-correlation technique for predicting the compressive buckling load of cylindrical shells under combined loading, Thin-Walled Struct. 216 (2025) 113576.
[43] F. Franzoni, A. Gliszczynski, T.D. Baciu, M.A. Arbelo, R. Degenhardt, Enhanced vibration correlation technique to predict the buckling load of unstiffened composite cylindrical shells, J. Sound Vib. 539 (2022) 117280.
[44] A.M.L. da Silva, F. Franzoni, G.C. B. Jr., Vibration correlation technique: methodology applied to buckling of large-scale sandwich cylindrical shell, Lat. Am. Appl. Res. 54 (3) (2024) 389–394.
[45] A. Gliszczynski, F. Franzoni, T.D. Baciu, R. Degenhardt, Evaluation of the stability and load-carrying capacity of double-curved unstiffened shells under compression through analysis of different initial imperfection sources, Aerosp. Sci. Technol. 168 (2026) 110907.
[46] A. Gliszczynski, F. Franzoni, R. Degenhardt, T.D. Baciu, VCT-Based Buckling load prediction in unstiffened CFRP cylinders: assessment of predictive robustness under varied imperfection maps and modifications to the arbelo characteristic chart, Compos. B: Eng. (2025) 113201.
[47] A. Gliszczynski, Effect of boundary conditions and analytical bifurcation load on VCT-based buckling load predictions for CFRP cylindrical shells, Compos. B: Eng. 312 (2026) 113317, ISSN: 1359–8368.
[48] J. William, Hughes Technical Center MMPDS-07: Metallic Materials Properties Development and Standardization (MMPDS), Federal Aviation Administration, Washington, DC, USA, 2012.
[49] J.G. Teng, X. Lina, J. Michael Rotter, X.L. Ding, Analysis of geometric imperfections in full-scale welded steel silos, Eng. Struct. 27 (2005) 938–950.
[50] E. Kreyszig, H. Kreyszig, E.J. Norminton, Advanced Engineering Mathematics, Wiley, Hoboken, NJ, USA, 2011.
[51] H.N.R. Wagner, C. Hühne, R. Khakimova, S. Niemann, M. Wang, J. Zhang, Structured chaos: redefining the design of buckling-critical cylindrical shells, Proc. R. Soc. A: Math. Phys. Eng. Sci. 481 (2321) (2025) 20250196.
[52] F. Franzoni, M.A. Arbelo, R. Degenhardt, Numerical assessment of existing vibration correlation techniques, in: Proceedings of the 15th European Conference on Spacecraft Structures, Materials and Environmental Testing, Noordwijk, NL, 2018.